

See discussions, stats, and author profiles for this publication at: <https://www.researchgate.net/publication/255963951>

Defect Thermodynamics and Diffusion Mechanisms in Li_2CO_3 and Implications for the Solid Electrolyte Interphase in Li-Ion Batteries

ARTICLE in THE JOURNAL OF PHYSICAL CHEMISTRY C · OCTOBER 2013

Impact Factor: 4.77 · DOI: 10.1021/jp310591u

CITATIONS

23

READS

165

4 AUTHORS, INCLUDING:



Yue Qi

Michigan State University

110 PUBLICATIONS 2,491 CITATIONS

SEE PROFILE



Hong Li

Chinese Academy of Sciences

277 PUBLICATIONS 10,718 CITATIONS

SEE PROFILE



Louis . Hector,

General Motors Company

194 PUBLICATIONS 3,500 CITATIONS

SEE PROFILE

MAY 2, 2013

VOLUME 117

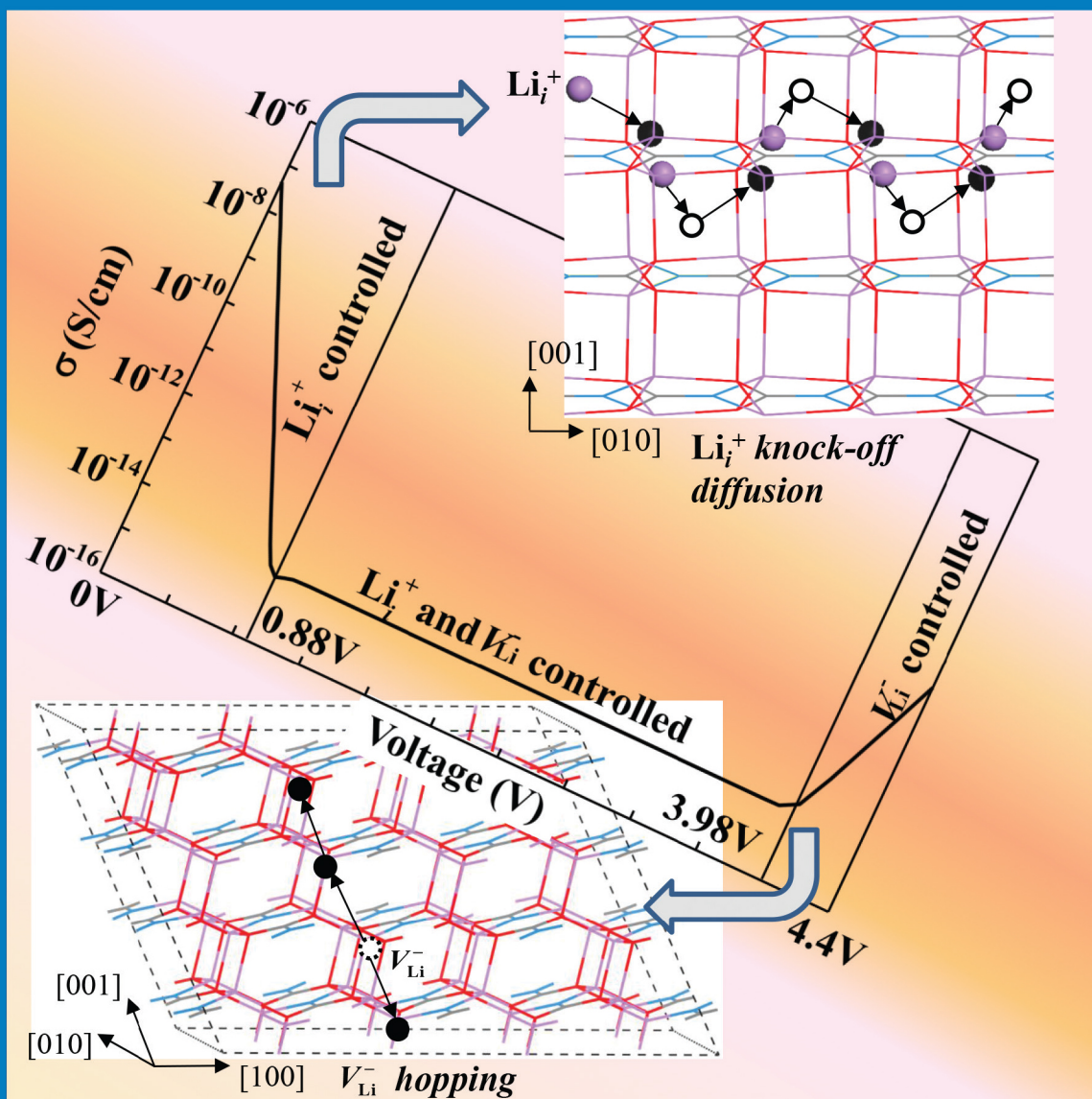
NUMBER 17

pubs.acs.org/JPCCK

THE JOURNAL OF PHYSICAL CHEMISTRY

C

Li Diffusion Carrier and Conductivity in Li_2CO_3 Mapped as a Function of Battery Voltage Based on First-Principles Calculations (see page 5A)



ENERGY CONVERSION AND STORAGE, OPTICAL AND ELECTRONIC DEVICES,
INTERFACES, NANOMATERIALS, AND HARD MATTER

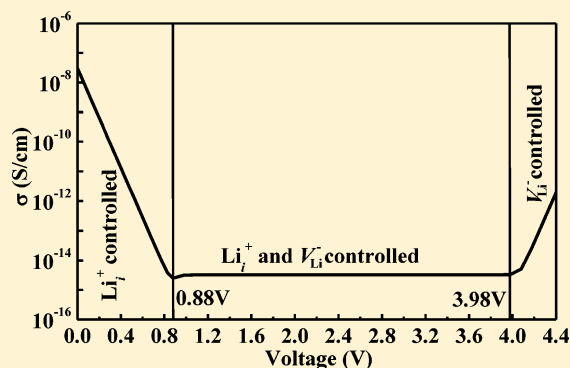


ACS Publications
MOST TRUSTED. MOST CITED. MOST READ.

www.acs.org

Defect Thermodynamics and Diffusion Mechanisms in Li_2CO_3 and Implications for the Solid Electrolyte Interphase in Li-Ion BatteriesSiqi Shi,^{†,||} Yue Qi,^{*,‡} Hong Li,[§] and Louis G. Hector, Jr.[‡][†]School of Engineering, Brown University, Providence, Rhode Island 02912, United States[‡]General Motors R&D Center, Warren, Michigan 48090, United States[§]Institute of Physics, Chinese Academy of Sciences, Beijing, 100190, China^{||}School of Materials Science and Engineering, Shanghai University, Shanghai 200444, China

ABSTRACT: Understanding and improving Li transport through crystalline Li_2CO_3 , a stable component of the solid electrolyte interphase (SEI) films in Li-ion batteries, is critical to battery rate performance, capacity drop, and power loss. Identification of the dominant diffusion carriers and their diffusion pathways in SEI films coated on anode and cathode surfaces is a necessary step toward the development of methods to increase Li conductivity. In this paper, we identify the dominant Li diffusion carriers in Li_2CO_3 over a voltage range (0–4.4 V) that includes typical anode and cathode materials by computing and comparing thermodynamics of all seven Li-associated point defects with density functional theory (DFT). The main diffusion carriers in Li_2CO_3 below 0.98 V are excess Li-ion interstitials; however, above 3.98 V, Li-ion vacancies become the dominant diffusion carrier type, and they have the same concentration in the voltage range of 0.98–3.98 V. Diffusion mechanisms of the main diffusion carriers were computed via the climbing image nudged elastic band method (CI-NEB). On the basis of the computed diffusion carrier concentration and diffusion barriers, the Li ionic conductivity was computed as a function of voltage, and it varies by ~ 5 orders of magnitude. Insights gained from our calculations allow us to suggest different dopants to enhance Li conductivity in SEI films and propose a new mechanism for electron leakage through an SEI film into the electrolyte. Li_2CO_3 is the one of the main stable components in the solid electrolyte interphase (SEI) in lithium-ion batteries and can be found in SEI films grown on both cathode and anode surfaces. On the basis of the concentrations and diffusion barriers computed for each of the identified point defects from first-principles calculations, the Li conductivity in Li_2CO_3 is mapped as a function of battery voltage. It is found that the diffusion carriers in the Li_2CO_3 on a negative electrode (graphite) are Li^+ interstitials but changed to Li^+ vacancies in the Li_2CO_3 coated on cathode materials. While Li^+ vacancies diffuse via a typical direct hopping mechanism, the excess Li^+ interstitials diffuse via repetitive knock-off with the Li^+ ions on lattice sites. The Li^+ interstitial conductivity in Li_2CO_3 on graphite is ~ 5 orders of magnitude faster than that of a Li^+ vacancy in Li_2CO_3 on the cathode. This suggests that Li transport through an SEI film on a cathode material can be dramatically different from Li transport through an SEI film on an anode material, despite the fact that SEI component chemistries appear to be similar in both cases. Thus, different doping strategies for the SEI on the anode and cathode could be taken to increase diffusion carrier concentrations in order to increase Li conductivity in an SEI film.



1. INTRODUCTION

Fluctuating oil prices, concerns about the adverse impact of hydrocarbon emissions on global climate change, and energy security are driving development of alternative energy storage technologies for transportation industries. The grand challenge for further development of Li-ion rechargeable batteries for electric vehicles is to simultaneously improve battery performance, life, cost, and abuse tolerance. Addressing these requirements is a difficult balancing act that has stimulated extensive effort devoted to discovery and synthesis of high capacity negative electrode materials (e.g., Sn, Si, and composites of Sn, Si, and graphite) and high voltage and capacity positive electrode materials (e.g., $\text{LiMn}_{1.5}\text{Ni}_{0.5}\text{O}_4$, LiCoPO_4 , LiNiPO_4 , Li_2MnO_3 , and $\text{Li}_2\text{FeSiO}_4$), as detailed in numerous reviews.^{1–6} At the same time, the oxidation and reduction potentials of battery

electrolytes, typically a mixture of organic solvents and salt components (e.g., LiPF_6 salt in solutions consisting of mixtures of ethylene carbonate (EC), dimethyl carbonate (DMC), and ethylmethyl carbonate (EMC) with additives), need to be well matched to the electrochemical potentials of the electrode materials. For example, the energy of the highest occupied molecular orbital (HOMO) of electrolyte molecules should be below the Fermi level of the positive electrode, while the lowest unoccupied molecular orbital (LUMO) must be higher than that of the negative electrode to ensure kinetically stable electrode/electrolyte interfaces.⁷ If the operating voltage of an electrode is

Received: October 25, 2012

Revised: February 19, 2013

Published: February 28, 2013

outside of the reduction and oxidation voltage range of the electrolyte, then it is necessary for the electrode surface to quickly develop a passivating film. This is the case for the graphite electrode, which is used in most commercial Li-ion batteries. During the initial charging of a Li-ion battery, components of the electrolyte are readily decomposed on pristine graphitic anodes. The decomposition products form an electronically passivating film on graphite surfaces, preventing further electrolyte reduction reactions. This passivating film does not preclude Li^+ transport from the electrolyte to the negative electrode; therefore, it is commonly referred to as the solid electrolyte interphase (SEI).^{8–13} Although commercially available cathode materials operate within the oxidation potential of the electrolyte, an SEI film may also cover the cathode surface.^{14–16} The formation of an SEI film on the cathode surface is a consequence of surface reactions with air (CO_2 and H_2O), reactions with the electrolyte, and/or ionic exchange processes. Clearly, electrode/electrolyte interfaces in Li-ion batteries are very complicated because both cathode and anode materials are covered by surface films. The overall transport step for a Li^+ ion in the electrolyte to insert into the electrode includes several steps in series, including Li^+ -ion transport, interfacial charge transfer, solid state diffusion, etc. Today the SEI is still claimed to be “the most important but the least understood (component) in rechargeable Li-ion batteries”.^{1,2,17}

Numerous studies over the past four decades have provided a comprehensive picture of SEI film chemistry and a general understanding of its formation mechanisms.^{8–13} The surface chemistry of SEI films has been probed with Fourier transform infrared (FTIR) spectroscopy, X-ray photoelectron spectroscopy (XPS), and energy-dispersive analysis by X-ray (EDAX) measurements, and morphological aspects have been revealed with scanning electron microscopy (SEM), atomic force microscopy (AFM), and scanning tunneling microscopy (STM). The general picture of the electrochemically formed SEI is that it is a mixture of inorganic salts (e.g., Li_2CO_3 , LiF , and Li_2O) near the SEI/electrode interface and organic salts (e.g., $(\text{CH}_2\text{OCO}_2\text{Li})_2$ and ROLi (R is an organic group that depends on the solvent) near the SEI/electrolyte interface.^{8,12,13,18} The most common failure modes (capacity drop or power loss) for Li-ion batteries involve SEI formation, growth, or loss of its electrical insulation character and Li^+ -ion transport properties. However, the extent to which SEI failure is determined by the chemical, morphological, physical, mechanical, or electrical changes in the film (or all of above) is poorly understood. This is mainly because far less emphasis has been devoted to correlating SEI film structure and properties despite the fact that the overall electrochemical behavior of SEI-covered electrodes has been measured by various techniques. Furthermore, most of these electrochemical methods are not well suited to extracting fundamental mechanical¹⁹ and transport properties about an SEI film since it is very thin (~ 10 – 50 nm) with a complex mosaic and heterogeneous structure.

Design of an artificial surface SEI film on cathode and anode materials in Li-ion batteries is an intriguing possibility. In fact, this topic has been the subject of many recent studies, with particular focus on higher capacity electrode materials (e.g., Si), nanostructured electrodes (high surface area), and high voltage cathode materials.^{7,20,21} Recently developed experimental techniques in which artificial SEI films are formed on electrode surfaces have led to improvements in the performance and the life of Li-ion batteries.^{22–24} However, the search for, the design of, and the synthesis of an optimal artificial SEI film material have

been hindered by the absence of structure–property relationships and an understanding of how such relationships impact Li-battery performance. Predictive modeling, starting from the ab initio level paired with carefully designed experiments, will accelerate the discovery of improved battery materials compared to doing theoretical or experimental work alone. The initial approach taken here is to start with individual SEI components that have been well-characterized by experiments and understand their properties (e.g., mechanical, transport, thermodynamics stability) to rationalize the differences between “good” and “bad” SEI components and then to provide design guidelines for artificial SEI material development (in fact, even the difference between “good” and “bad” is unknown).

As a significant step toward this goal, the present study focuses on Li_2CO_3 , one of the most chemically stable SEI components, since it plays a major role in stabilizing SEI films.²⁵ Li_2CO_3 has been reported to appear in SEI films formed on both cathode and anode surfaces.^{7,14,25–29} In particular, observations of crystalline Li_2CO_3 are detailed in the following experimental studies: on graphite surfaces after cycling (with TEM);^{29–31} in an SEI film formed on a Cu current collector at 0.4 V (using transmission electron microscopy (TEM) and time-of-flight secondary-ion mass spectrometry (TOF-SIMS));^{32,33} and on a $\text{Li-Ni}_{1-x}\text{Co}_x\text{Al}_y\text{O}_2$ surface after storage in air due to surface reaction with CO_2 (using TEM¹⁴ and X-ray³⁴). Its structure and thermodynamics have been reported in studies in the extant literature, some of which are unrelated to Li-ion batteries.^{35–38} Concentrations of various Li diffusion carriers and Li diffusion coefficients in Li_2CO_3 on a negative electrode and the mechanical properties of Li_2CO_3 have been computed to understand Li transport and mechanical stability for Li-ion battery applications.^{32,39–41}

Li^+ -ion diffusion in Li_2CO_3 is likely to be the rate-controlling process for Li^+ transport through an SEI film, since the Li_2CO_3 phase is the primary component of the dense layer formed near an electrode surface. However, the mechanism of Li transport through the Li_2CO_3 phase has been the subject of some debate. For example, Mizusaki et al.⁴² claimed that crystalline Li_2CO_3 is a pure Li^+ conductor. Their measured Li diffusivity and estimated Li interstitial concentration were subsequently used by Christensen and Newman to model SEI growth on a graphite anode assuming that the entire SEI film consisted of pure Li_2CO_3 .⁴³ Li_2CO_3 has also been proposed for use as a solid electrolyte for CO_2 sensors based on the idea that it is Li-conductive.⁴⁴ However, Zhuang et al.¹⁴ showed strong evidence of particle isolation that resulted from the formation of Li_2CO_3 on $\text{LiNi}_{1-x}\text{Co}_x\text{Al}_y\text{O}_2$ (NCA) particles. In their study, some NCA particles could not be lithiated/delithiated after the surface was covered with Li_2CO_3 ; however, it is not clear if this was a result of Li_2CO_3 blocking Li^+ transport or electronic transport. Kobayashi et al.⁴⁵ also attributed power fading of NCA to the formation of a surface layer containing Li_2CO_3 . These observations might be the reasons why Winter¹⁷ argued that Li_2CO_3 does not transport Li^+ ions. It seems that whether or not Li_2CO_3 conducts Li is strongly dependent upon which material (i.e., anode or cathode) is coated with an SEI film. The ionic conductivity is controlled by the point defects (e.g., interstitials, vacancies) in materials.

In our previous study of Li diffusion in Li_2CO_3 , we computed formation energies for all seven point defects in crystalline Li_2CO_3 using first-principles density functional theory (DFT).³² We formulated the formation energies of these defects as a function of the chemical potential of Li, assuming that the Li in a thin Li_2CO_3 film is in equilibrium with the Li in the electrode

Table 1. Lattice Parameters (a , b , c , and β) and Band Gap (E_g) of Li_2CO_3 ^a

	LDA (this study)	GGA-PBE (this study)	exptl (ref 50, 298 K)
a (Å)	8.249	8.442	8.359
b (Å)	4.906	5.047	4.974
c (Å)	5.847	6.356	6.194
β (°)	114.553	114.629	114.789
Li(8f)	(0.1944, 0.4441, 0.8320)	(0.1987, 0.4474, 0.8372)	(0.1968, 0.4454, 0.8334)
C(4e)	(0.0, 0.0679, 0.25)	(0.0, 0.0662, 0.25)	(0.0, 0.0665, 0.25)
O(I)(4e)	(0.0, 0.3273, 0.25)	(0.0, 0.3209, 0.25)	(0.0, 0.3213, 0.25)
O(II)(8f)	(0.1474, -0.0648, 0.3108)	(0.1469, -0.0635, 0.3144)	(0.1463, -0.0631, 0.3133)
E_g (eV)	4.868	5.04	

^a4e and 8f represent the Wyckoff parameters of atomic species.

which it coats. The chemical potential of Li in an electrode material is directly related to the open circuit voltage of that electrode material with respect to Li metal (Li^+/Li). Therefore, the formation energy of each Li-related defect was computed as a function of voltage. We concluded that Li-ion interstitials are the dominant carriers in Li_2CO_3 in the voltage range of 0–0.8 V (for example on a graphite anode).³²

The present study was motivated by our hypothesis that the Li defect formation energy in Li_2CO_3 is strongly influenced by the Li chemical potential in the electrode that the Li_2CO_3 coats.³² This becomes even more important as Li_2CO_3 can form on both anode and cathode surfaces. We expand on our previous investigation of Li diffusion in crystalline Li_2CO_3 by extending the voltage range from 0 to 4.4 V. This allows us to identify the dominant diffusion carriers in Li_2CO_3 on typical cathode materials (such as NCA) as a function of battery cell voltage. On the basis of the concentration and diffusion barriers computed for each of the identified point defects, the Li conductivity in Li_2CO_3 is mapped as a function of battery voltage. In contrast to our previous finding that the diffusion carriers in Li_2CO_3 on graphite are Li^+ interstitials,³² we find that Li^+ vacancies are the dominant diffusion carriers in Li_2CO_3 coated on NCA. The Li-ion interstitial conductivity in Li_2CO_3 on graphite is ~ 5 orders of magnitude faster than that of a Li-ion vacancy in Li_2CO_3 on NCA. This suggests that Li transport through an SEI film on a cathode material can be dramatically different from Li transport through an SEI film on an anode material, despite the fact that SEI component chemistries appear to be similar in both cases (as noted above, Li_2CO_3 is found in SEI films grown on both cathode and anode surfaces). We also found that neutral Li interstitials, Li_i^0 , become the second highest concentrated defects in Li_2CO_3 at a very low voltage behind Li_i^+ . Both Li_i^0 and Li_i^+ diffuse by knocking off the Li^+ ion from a lattice site rather than direct hopping through empty channels between lattice sites with their ~ 0.3 eV diffusion barrier. When Li_i^0 diffuses, its associated electron is distributed on the nearby C atoms and diffuses along with the Li^+ , providing a new mechanism for electron leakage through the SEI into the electrolyte. This mechanism offers a possible explanation as to why the SEI can grow thicker than the normal electron tunneling length, and significant self-discharge of the lithiated anode occurs at low voltage. On the one hand, these insights provide direct and clear directions toward promising dopant materials that are likely to increase Li conductivity by increasing diffusion carrier concentrations in SEI films. Examples are BO_3^{3-} replacing CO_3^{2-} which will increase Li-ion interstitial concentration and Ca^{2+} or/and NO_3^- doping which will increase Li-ion vacancies. This opens up the possibility of synthesizing or modifying SEI

films with enhanced Li conductivity in new Li-ion battery designs.

2. COMPUTATIONAL DETAILS

All calculations in this study were based upon the implementation of plane wave DFT in the Vienna ab initio simulation package (VASP).⁴⁶ Potentials constructed with the full potential projector augmented wave (PAW) method⁴⁷ were used for the elemental constituents. The exchange-correlation part of the density functional was treated within the local density approximation (LDA).^{48,49} Valence electron configurations for the elemental constituents were as follows: Li-1s²2s¹, C-2s²2p², and O-2s²2p⁴. Prior to the defect calculations, all structural parameters (lattice parameters and nuclear coordinates) in the monoclinic Li_2CO_3 (C2/c, No.15, $Z = 4$) conventional cell⁵⁰ were optimized by simultaneously minimizing the Hellmann–Feynman force components to 0.01 eV/Å. For this purpose, a 520 eV cutoff energy for the plane-wave basis was chosen along with a $2 \times 4 \times 3$ Monkhorst–Pack⁵¹ k -point mesh with Gaussian smearing and a 0.2 eV energy broadening. This set of parameters assured that total energies converged to at least 10^{-7} eV/unit cell. We also conducted ancillary GGA calculations within the Perdew–Burke–Ernzerhof (PBE) functional,⁵² and listed our comparisons in Table 1. Phonon calculations were conducted with the conventional supercell approach (in the PHONON code developed by Parlinski as implemented in the MedeA environment^{53,54}). These provided vibrational properties of Li_2CO_3 (perfect and with defects) and allowed us to explore the vibrational stability of structures associated with the transition state calculations. We did not account for the LO–TO zone center splitting since these have previously been shown to have negligible influence on thermodynamic calculations with DFT.⁵⁵

To understand Li transport in Li_2CO_3 , only Li-related point defects with different charge states are considered since the CO_3^{2-} group is covalently bonded and its size dramatically exceeds that of Li^+ . Here, the following defect definitions apply: V_{Li} (neutral Li vacancy); V_{Li}^- (negatively charged Li vacancy); Li_i^0 (excess interstitial Li atom); Li_i^+ (excess interstitial Li ion); Li_{FP} (neutral Li Frenkel pair); Li_{FP}^+ (positively charged Li Frenkel pair); Li_{FP}^- (negatively charged Li Frenkel pair). We model point defect properties using an as-built $2 \times 2 \times 2$ supercell constructed from the fully VASP-optimized Li_2CO_3 conventional cell geometry. This is sufficient to isolate the defect from its periodic images and hence simulate a dilute defect concentration. For the same point defect in a $2 \times 2 \times 4$ supercell, our first-principles calculations predict that the distorted lattice structure due to the presence of the point defect is identical to that obtained with the $2 \times 2 \times 2$ supercell. To simulate a charged point defect in a $2 \times 2 \times 2$ supercell, a jellium background charge

was first added and then subtracted (by assuming a dielectric constant of one) to neutralize the supercell for computational efficiency.⁵⁶

Following Zhang and Northrup,⁵⁷ the formation energy with a defect i at charge state q is defined as

$$E_f(i, q) = E_{\text{tot}}(i, q) - E_{\text{tot}}(\text{Li}_2\text{CO}_3, \text{bulk}) - n_{\text{Li}}\mu_{\text{Li}} + q(\varepsilon_F + E_V) \quad (1)$$

where $E_{\text{tot}}(i, q)$ and $E_{\text{tot}}(\text{Li}_2\text{CO}_3, \text{bulk})$ are the total energies of the supercell with one (charged) defect i and an equivalent, defect-free supercell, respectively. The number of Li atoms (ions) added to ($n_{\text{Li}} > 0$) or removed from ($n_{\text{Li}} < 0$) the perfect (i.e., defect-free) Li_2CO_3 supercell when defects are generated is n_{Li} , and the chemical potential of Li is μ_{Li} . The Fermi level, ε_F , relative to the valence-band maximum in the bulk, E_V , changes with defect concentration and can be computed by imposing the following charge neutrality condition

$$\sum_i q(i)S(i, q) = n_e - n_h \quad (2)$$

where $q(i)$ and $S(i, q)$ are the charge and the concentration of each defect i , respectively, and n_e and n_h are the concentrations of free electrons and holes, respectively. At thermodynamic equilibrium, the concentration of each defect i at charge state q in a crystalline material is

$$S(i, q) = N_s(i)e^{-E_f(i, q)/k_B T} \quad (3)$$

where $E_f(i, q)$ is the formation energy of defect i at charge state q in eq 1, and $N_s(i)$ is the number of sites where defect i can be generated per unit volume. Boltzmann's constant is k_B , and T is the temperature (300 K in our calculations). In a defect-free Li_2CO_3 , the concentrations of free electrons (n_e) and holes (n_h) are equal

$$n_e = n_h = (N_C N_V)^{1/2} e^{(-E_g/2k_B T)} \quad (4)$$

Here, N_C (N_V) and E_g are the effective density of states of the conduction (valence) band and band gap of defect-free Li_2CO_3 , respectively. For a Li_2CO_3 crystal with defects, the carrier concentrations depend on ε_F as follows

$$n_e = N_C e^{[-(E_g - \varepsilon_F)/k_B T]}, \quad n_h = N_V e^{(-\varepsilon_F/k_B T)} \quad (5)$$

To maintain charge neutrality, ε_F can be determined by solving the following equation for each given μ_{Li} value

$$\sum_i q(i)N_s(i)e^{[-E_f(i, q)/k_B T]} = N_C e^{[-(E_g - \varepsilon_F)/k_B T]} - N_V e^{(-\varepsilon_F/k_B T)} \quad (6)$$

Note that μ_{Li} is referenced to the bulk energy, $\mu_{\text{Li}}^{\text{metal}}$, of Li metal, and it is thus related to the voltage in a Li-ion battery by setting the electrochemical potential of Li metal (Li^+/Li) to be 0. Therefore

$$V = -(\mu_{\text{Li}} - \mu_{\text{Li}}^{\text{metal}})/e \quad (7)$$

where V is in volts and μ_{Li} is in eV. Equation 7 gives the open circuit voltage of the electrode which is coated with a Li_2CO_3 layer. It provides the dependence of the defect formation energy and the defect concentration on the voltage of the battery electrode materials.

To determine Li-ion diffusion barriers and paths, the climbing image nudged elastic band method (CI-NEB),⁵⁸ with VASP as

the computational engine, was used to compute transition state structures. For this purpose, a chain of three initial images was chosen between two end-point structures; the images were created by linearly shifting the moving atoms between the starting and ending structures. The energy was minimized in all directions except for the direction of the reaction pathway. After the CI-NEB calculations, a final geometry optimization was conducted on the transition state structure with the VASP implementation of the residual minimization–direct inversion in the iterative subspace (RMM–DIIS) algorithm.⁵⁹ Here, only forces and not the total energy are minimized. This helps to prevent the transition state structure from falling back down the energy barrier provided that the starting transition state structure is close to or at the optimized transition state. A phonon calculation on each transition state structure revealed a single imaginary frequency, as expected.

3. RESULTS AND DISCUSSION

3.1. Perfect Li_2CO_3 Crystal. Before we discuss defects in Li_2CO_3 , it is necessary to review some details of the perfect Li_2CO_3 crystal structure. Figure 1 shows that planar CO_3^{2-}

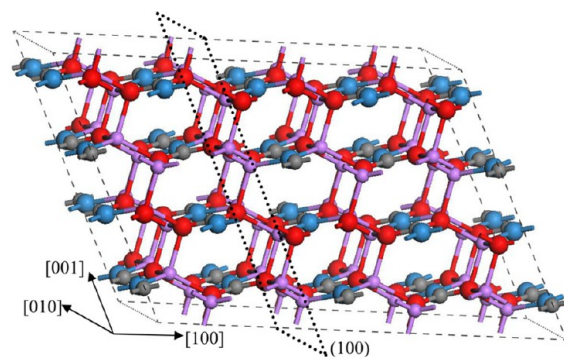


Figure 1. Monoclinic Li_2CO_3 ($C2/c$, No.15, $Z = 4$) shown as a $2 \times 2 \times 2$ supercell. Computed lattice parameters from LDA are: $a = 8.249 \text{ \AA}$, $b = 4.906 \text{ \AA}$, $c = 5.847 \text{ \AA}$, and $\alpha = \gamma = 90^\circ$, $\beta = 114.553^\circ$ (each is within 2.5% of experimental values at 298 K⁵⁰). Li, C, O(I), and O(II) atoms at the lattice sites are represented by purple, gray, blue, and red spheres, respectively.

anions form building blocks parallel to the (100) plane (highlighted by the black dotted region) by aligning along [010] and stacking in a zig-zagged fashion along [001]. Such blocks, which are shifted by one-half of the distance between planar CO_3^{2-} anions along [001], stand side-by-side along [100]. Li^+ ions are situated between these blocks, mainly within the (100) plane. The three C–O bonds are not equal and can be separated into two groups: one O(I) (blue sphere) with a 1.272 \AA C–O(I) bond length and two O(II) (red sphere) with a 1.292 \AA bond length. The C–O(I) bonds are oriented along either [010] or [0 $\bar{1}$ 0] directions. Furthermore, the O(I) is bonded to two Li ions at a distance of 1.849 \AA , whereas the O(II) is bonded to three Li^+ ions at distances of 1.894, 1.912, and 1.950 \AA . Consequently, each Li^+ in the Li_2CO_3 lattice is tetrahedrally coordinated with one O(I) and three O(II). Note that C–O and Li–O distances refer to our VASP calculated values.

Table 1 summarizes our computed (LDA and GGA-PBE) Li_2CO_3 lattice parameters and band gap together with calculated and experimental results from the extant literature. The lattice parameters from LDA are within 2.5% of room-temperature measurements.⁵⁰ The computed Li_2CO_3 band gap is 4.868 eV

from LDA and 5.04 eV from GGA. Since LDA and GGA tend to underestimate the band gap, in the absence of experimental value, the use of HSE06 hybrid functions provides the most rigorous quantitative result, which is 7.07 eV. This large band gap and the highly localized covalent C–O bonds and ionic Li–O bonds suggest that Li_2CO_3 is electronically insulating. Analyses of site-projected density of states and charge density difference contours (not shown) suggest that C–O bonds are covalent and Li^+ (referring to both lattice Li^+ and excess interstitial Li^+ as discussed below) is ionically bonded to O ions.

Experimentally measured mechanical property data such as elasticity tensor components (C_{ij}) and polycrystalline moduli are not available due to the difficulty of growing a Li_2CO_3 crystal of sufficient size. However, we previously reported VASP-computed results from lattice dynamics, thermodynamics, and elastic properties of monoclinic Li_2CO_3 .⁴¹ These results lead to the conclusion that the perfect Li_2CO_3 lattice is both mechanically and vibrationally stable.

3.2. Defect Thermodynamics, Structure, and Diffusion in Li_2CO_3 . 3.2.1. Overview of the Diffusion Carriers.

After computing the total energies of supercells with all seven point defects and an equivalent defect-free supercell, we can derive the dependence of our computed $E_f(i,q)$ and $S(i,q)$ on the voltage using eqs 1–7 at 300 K. These quantities are plotted within the voltage range of typical Li-ion batteries, i.e., 0–4.4 V, in Figures 2(a) and 2(b) along with the n_e and n_h concentrations. For a graphite negative electrode, the typical voltage of SEI film

formation starts at 0.8 V;⁶⁰ Li intercalation begins below the SEI formation voltage and continues until the formation of fully intercalated graphite, LiC_6 , at a computed voltage of ~ 0.3 V.⁶¹ The 0.3 and 0.8 V quantities are highlighted as dotted vertical lines in Figures 2(a) and 2(b) to facilitate our discussion of defects in Li_2CO_3 on a graphite anode. Note that the computed LiC_6 formation voltage is higher than the experimental value of ~ 0.1 V⁶² due to the overestimation of Li–C binding in LiC_6 with LDA.

Figure 2(a) shows that in the 0.0–0.98 V range the positively charged excess interstitial Li ion, Li_i^+ , exhibits the lowest formation energy (0.34–0.81 eV). Consequently, its concentration is the highest, ranging from 2.34×10^{16} to 9.00×10^8 cm^{-3} , among all the defects shown in Figure 2(b). In this voltage range, charge neutrality is mainly maintained by the equal concentration of Li_i^+ and free electrons. Note that Li_2CO_3 is still an ionic conductor and electronic insulator even when the n_e concentration is the same as Li_i^+ , due to the large band gap and very localized electron distribution around the Fermi level (according to the electronic density of states). Initially, the formation energy for Li_i^+ increases and V_{Li}^- decreases with voltage; however, beyond 0.98 V, Li_i and V_{Li}^- exhibit the same lowest formation energy, 0.81 eV. Our calculations show that Li_i^+ is the main diffusion carrier only at low voltages (e.g., 0–0.8 V) (a typical range for a negative electrode). We note that Christensen and Newman⁴³ used a continuum-scale mathematical model to study SEI growth on graphite, by assuming that Li_i^+ is the main defect in Li_2CO_3 with a concentration of $6 \times 10^{18} \sim 3 \times 10^{19}$ cm^{-3} , close to the computed value at near zero voltage.

For a typical transition metal oxide electrode, the voltage is above 2.5–4.5 V. For the Li_2CO_3 layer in a cathode SEI film, the typical voltage is above 2.5 V. Clearly, the diffusion carriers in Li_2CO_3 change from low voltage to high voltage, and thus either both Li_i^+ and V_{Li}^- or V_{Li}^- become the dominant diffusion carriers in Li_2CO_3 on a cathode surface. The equal concentrations of Li_i^+ and V_{Li}^- maintain overall charge neutrality for voltages from 0.98 to 3.98 V. Above 3.98 V, V_{Li}^- has the highest concentration and hence it is the dominant diffusion carrier, while charge neutrality is maintained with holes. Wang et al.⁶³ have shown that Li_2CO_3 can decompose above ~ 4.1 V if the catalyst exists; we therefore limit the voltage range of interest in this study to 0–4.4 V. The transition of the main diffusion carriers from Li_i^+ at low voltage (below 0.98 V) to V_{Li}^- at high voltage (above 3.98 V) is also due to balancing Li and electron chemical potentials. Clearly, LDA underestimates band gaps, but the hybrid functional predicts a 40% higher band gap. This will lead to lower electron and Li_i^+ concentrations but similar hole and V_{Li}^- concentrations, while in general the dependence of the transition of the main diffusion carriers on voltage will remain the same.

Experiments on single crystal Li_2CO_3 (instead of a thin film on an electrode) have concluded that Li^+ conduction is essentially by the interstitial Li^+ ions and not by Li vacancies.⁴² We expect that the Li chemical potentials for bulk Li_2CO_3 and a thin film of Li_2CO_3 in conjunction with an electrode particle are not always the same. Figures 2(a) and 2(b) show that only the formation energy of the Frenkel pair does not depend on voltage (or Li chemical potential) since its formation does not change the number of Li atoms in the system. Our computed formation energy of 1.121 eV for a neutral Li Frenkel pair is in good agreement with that (1.136 eV) reported in experiments on Li-ion diffusion in bulk Li_2CO_3 by Mizusaki et al.⁴² but lower than another DFT computed formation energy of 1.7 eV.³⁹

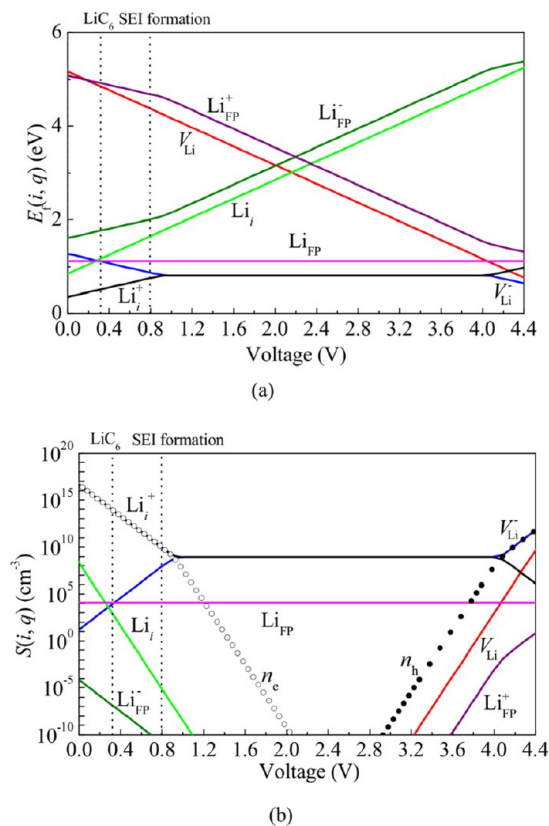


Figure 2. (a) Formation energies, $E_f(i,q)$, for all seven point defects. (b) The defect concentrations, $S(i,q)$, for the five defects with the lowest $E_f(i,q)$ are shown. Both figures are calculated as a function of voltage. The two vertical dotted lines in (a) and (b) correspond to the voltage for the formation of (from left to right) LiC_6 and SEI on the surface of a negative electrode.

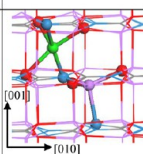
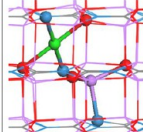
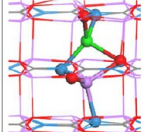
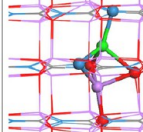
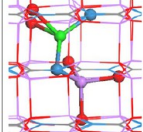
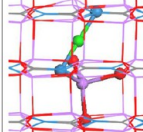
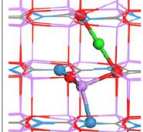
A Li Frenkel pair, Li_{FP} , becomes the third most energetically favorable diffusion carrier (after Li_i^+ and V_{Li}^-) above 0.38 V. In the 0.0–0.28 V range, the secondary diffusion carrier is the neutral interstitial Li atom, Li_i (after Li_i^+), with a formation energy within 0.88–1.13 eV and concentration within $5.42 \times 10^7 \sim 3.94 \times 10^3 \text{ cm}^{-3}$ (as compared with $2.34 \times 10^{16} \sim 1.99 \times 10^{14} \text{ cm}^{-3}$ for Li_i^+ in the same range). According to Figures 2(a) and 2(b), V_{Li}^- is the second most energetically favored diffusion carrier, in the voltage range from 0.28 to 0.98 V, with the formation energy of 1.13–0.81 eV within the $3.72 \times 10^3 \sim 8.23 \times 10^8 \text{ cm}^{-3}$ concentration range. Below 4.4 V, V_{Li} does not become a dominant diffusion carrier in Li_2CO_3 although its hopping energy barrier along [001] is only 0.23 eV as shown in ref 40.

So far, we have considered Li_2CO_3 as a bulk material, and its Fermi level is determined by the intrinsic defects. In Li-ion batteries, the Fermi level of the thin SEI film can be changed by the conductive phase it covers. Fixing the chemical potential of Li (or the voltage) and tuning the Fermi level will also lead to the same dominating diffusion carriers; however, we notice that lowering the Fermi level on the negative electrode side will increase the concentration of Li_i^+ , while raising the Fermi level on the positive electrode side will increase the concentration of V_{Li}^- .

3.2.2. Structure and Diffusion Pathways of the Main Diffusion Carriers in Li_2CO_3 . A. Li-Ion Interstitials. There are many possible interstitial Li^+ sites in the monoclinic Li_2CO_3 crystal structure. It is therefore necessary to first locate the energetically favorable configuration for each Li^+ site before we consider the corresponding diffusion mechanism. Table 2 lists the relaxed Li_i^+ configurations, along with the VASP-computed total energies with respect to Conf. 1 and the distances between interstitial Li^+ and nearby O. It is evident that a higher O-coordination number corresponds to a lower formation energy for Li_i^+ interstitials. The 5-fold coordinated interstitial site in Conf. 1 is the most energetically favorable configuration. This 5-fold O coordination pattern of the Li_i^+ ion in Conf. 1 is associated with two Li–O(I) and three Li–O(II) bonds (interstitial bond lengths are listed in Table 2). The formation energies for 4-fold coordinated interstitial configurations, as shown in Confs. 2–5, are 0.0432–0.5296 eV higher than that of Conf. 1. The 4-fold coordinated interstitial Li–O bond lengths (two Li–O(I) bonds and two Li–O(II) bonds) in Confs. 2–4 are very close to those in the perfect Li_2CO_3 crystal, where the lattice Li^+ ion is coordinated with one Li–O(I) and three Li–O(II). We believe that Conf. 3 is identical to the interstitial equilibrium configuration discussed in ref 39. The two sites with only 2-fold O coordination (two Li–O(I) for Conf. 6 and two Li–O(II) for Conf. 7) have the largest excess volume (which is the space left in between Voronoi cells generated around each atom based on the atomic radius) in crystalline Li_2CO_3 relative to other sites. However, they show even higher energies of 0.7644–0.8749 eV above Conf. 1. The locations of excess interstitial Li^+ at the center of the open spaces in the Li_2CO_3 lattice are least favored in Confs. 6 and 7. This runs counter to intuition that would suggest excess interstitial Li^+ locates within the largest open space as shown in Confs. 6 and 7. This further confirms that the higher the O coordination number of the interstitial Li ion, the more energetically favorable is the system. Hence, the Li_i^+ formation energy, its concentration in Figure 2, and the diffusion mechanism are all based on the 5-fold coordinated site in Conf. 1 as the most energetically favorable site.

The incorporation of excess interstitial Li_i^+ into the Li_2CO_3 lattice leads to a structural distortion, and the distortion is mainly localized on the neighboring lattice Li^+ in the (100) plane. For

Table 2. Energy and Interstitial Li–O Bond Length Parameters for Different Interstitial Li^+ Configurations in Li_2CO_3 ^a

Label	Direct coordinates of interstitial site	Energy (eV)	Number of perturbed lattice Li^+ ions	Interstitial Li–O bond lengths (Å)	Atomic configuration of interstitial model
Conf. 1	(0.3672,0.362,0.7656)	0	3: 2×O(I), 2×O(II) 2×O(I), 2×O(II), 2×O(I), 2×O(II)	Li–O(I): 2.017, 2.024 Li–O(II): 1.956, 1.956, 1.961	
Conf. 2	(0.375,0.375,0.75)	0.0432	2: 2×O(I), 2×O(II) 2×O(I), 2×O(II)	Li–O(I): 1.992, 1.992 Li–O(II): 1.939, 1.939	
Conf. 3	(0.3043,0.5423,0.7467)	0.218	1: 2×O(I), 2×O(II)	Li–O(I): 1.836, 1.909 Li–O(II): 1.853, 1.979	
Conf. 4	(0.4434,0.7847,0.7222)	0.3373	2: 2×O(I), 2×O(II) 1×O(I), 3×O(II)	Li–O(I): 1.820, 1.947 Li–O(II): 1.875, 2.091	
Conf. 5	(0.2403,0.4275,0.7772)	0.5296	0	Li–O(I): 1.822, 1.831 Li–O(II): 1.998, 2.019	
Conf. 6	(0.25,0.5,0.75)	0.7644	0	Li–O(I): 1.786, 1.786	
Conf. 7	(0.375,0.625,0.75)	0.8749	2: 2×O(I), 2×O(II) 2×O(I), 2×O(II)	Li–O(II): 1.745, 1.745	

^aInterstitial Li, lattice Li, C, O(I), and O(II) atoms are represented by green, purple, gray, blue, and red spheres (lines), respectively. Coordinates of the interstitial site are given as fractional coordinates of the $2 \times 2 \times 2$ perfect crystal structure supercell in Figure 1. Energy is relative to the energy of Conf. 1 in units of eV. Perturbed lattice Li^+ ion refers to that with the movement (relative to its site in the perfect crystal) exceeding 0.352 Å. The energy of the most stable interstitial Li^+ configuration is set to 0 eV.

example, in Conf. 1, three lattice Li^+ ions in the same (100) layer are displaced from their original lattice sites by 1.086, 0.877, and 0.820 Å due to the excess interstitial Li_i^+ . Note that this displacement mainly occurs along the [001] direction, resulting in the breaking of one Li–O(II) bond and the formation of one new Li–O(I) bond. In other words, each perturbed lattice Li^+ is coordinated by two O(I) and two O(II) ions as shown in Table 2. Positions of all other atoms are only slightly changed (i.e., displacements relative to their positions in the perfect Li_2CO_3 lattice are within 0.289 Å), and other lattice Li^+ ions remain 4-fold coordinated with O. This structural distortion, which mainly occurs along [001] in the (100) layer, is also consistent with our previous results that both elasticity tensor components C_{11} and C_{22} of the perfect Li_2CO_3 structure are about two to three times

larger than C_{33} due to the zig-zagged layer structure perpendicular to $[001]$.⁴¹

The diffusion mechanism associated with the excess interstitial Li_i^+ ion in Li_2CO_3 has been reported in our previous study.³² In summary, the excess interstitial Li^+ ion diffuses via a repetitive knock-off with lattice Li^+ sites within the (100) plane rather than via direct hopping through spaces between the lattice sites. The energy barriers for the repetitive *knock-off* and *direct-hopping* diffusion mechanisms along the $[010]$ direction are 0.31 and 0.54 eV, respectively. The lower energy barrier for the knock-off mechanism is due to the stable coordination environment maintained during diffusion in which each Li^+ coordinates with five O ions. In this study, we recomputed the diffusion pathway using the GGA-PBE functional, and the energy barrier for the knock-off mechanism is dropped to 0.24 eV.

B. Li-Ion Vacancies. V_{Li}^- has the same concentration as Li_i^+ above 0.98 eV, and it therefore becomes one of the main diffusion carriers in a Li_2CO_3 layer as part of an SEI film on a cathode surface, as shown in Figure 2. Thus, it is necessary to examine its formation and diffusion behavior. A single, negatively charged Li vacancy, V_{Li}^- , is generated by removing one lattice Li^+ from a $2 \times 2 \times 2$ Li_2CO_3 supercell (equivalent to removing one lattice Li^0 atom and adding a negative charge to the supercell). After atomic relaxation, only one neighboring lattice Li in the (100) plane moves mainly along $[001]$ toward the Li vacancy by 0.884 Å, while all other atoms are only slightly disturbed (movements relative to their positions in the perfect Li_2CO_3 lattice are within 0.397 Å). All Li ions are tetrahedrally coordinated with O ions.

Li^+ -ion diffusion through the crystalline Li_2CO_3 lattice is achieved by its repetitively switching position with a nearby V_{Li}^- and vice versa. Figure 3(a) schematically shows all possible diffusion pathways for V_{Li}^- in the perfect Li_2CO_3 lattice. There are five different pathways for a V_{Li}^- to switch positions with its neighboring lattice Li^+ . These pathways are labeled as (1)–(5). The distance between the V_{Li}^- and Li^+ in the perfect Li_2CO_3 lattice changes after atomic relaxation. We listed the distance in both the perfect crystal and the structure after atomic relaxation (the actual diffusion distance per step) in Table 3. Because the neighboring lattice Li^+ in the (100) plane along the approximate $[001]$ direction has already moved toward the V_{Li}^- by 0.884 Å after atomic relaxation, its diffusion distance along $[001]$ is therefore shortened from 2.974 to 2.175 Å. Thus, lattice distortion caused by the formation of V_{Li}^- renders the diffusion length along $[001]$ (pathway (1)) the shortest relative to all other diffusion directions.

Figure 3(b) shows the corresponding energy profiles along pathways (1)–(5). For comparison, Table 3 also lists the energy barriers and the Li–O bond lengths associated with the moving Li^+ when it switches position with V_{Li}^- at the transition state. The pathway (1), which can be characterized by diffusion along the $[001]$ direction in the (100) plane, exhibits the lowest energy barrier of 0.235 eV. Pathways (2) and (3) have the next lowest energy barrier of 0.394 eV, which are associated with $[010]$ and $[100]$ motion in the (001) plane, respectively. For pathway (4) along the $[01\bar{1}]$ direction, the diffusion distance is the longest (3.553 Å) compared with other pathways, resulting in a much higher energy barrier of 0.492 eV. For pathway (5) along the $[0\bar{1}1]$ direction, diffusion must go through the transition state where Li^+ is only coordinated with two O^{2-} ions, resulting in the highest energy barrier (0.683 eV). Although the diffusion distance for pathway (5) is only 0.205 Å longer than that for the pathway (1), the energy barrier of the former is about three times higher than the latter because of the lower coordination

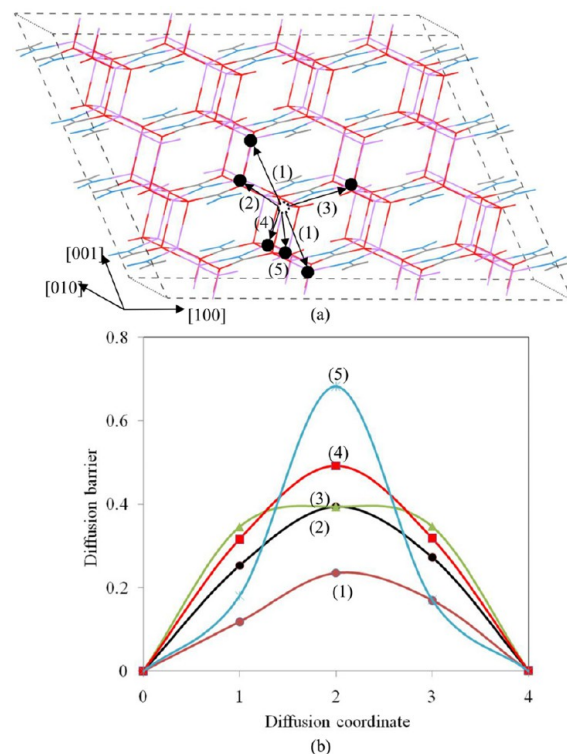


Figure 3. (a) Schematic diagram of the V_{Li}^- diffusion pathways. (b) Energy profiles of the V_{Li}^- diffusion pathways in (a) from CI-NEB. Li, C, O(I), and O(II) atoms at the lattice sites are represented by purple, gray, blue, and red lines, respectively. Hollow and black spheres mark, respectively, the site of the V_{Li}^- and the sites through which V_{Li}^- diffuses. (b) Lines (1)–(5) denote the corresponding diffusion energy profiles of the V_{Li}^- along diffusion pathways (1)–(5) in (a).

Table 3. Energy Barriers, Net Distances between Adjacent Lattice Sites in the Perfect Li_2CO_3 , Lattice Diffusion Distance Per Step, and Li–O Bond Lengths at the Transition State for the Five Pathways for V_{Li}^- Diffusion Shown in Figure 3(a)

pathway ^a	energy barrier (eV)	net distance ^b (Å)	diffusion distance per step (Å)	Li–O bond lengths at transition state (Å)
(1)	0.235	2.974	2.175	Li–O(I): 1.833, 2.393 Li–O(II): 1.829, 1.927
(2)	0.394	2.917	2.753	Li–O(I): 2.151, 2.162 Li–O(II): 1.784, 1.902
(3)	0.394	2.940	2.743	Li–O(I): 1.686 Li–O(II): 1.910, 1.915
(4)	0.492	3.494	3.553	Li–O(I): 1.952, 1.955 Li–O(II): 2.010, 2.015
(5)	0.683	2.613	2.380	Li–O(II): 1.767, 1.774

^aLabels defined in Figure 3. ^bDistances as measured from the corresponding perfect crystal sites before VASP relaxation.

number for the diffusing Li^+ with O^{2-} ions at the transition state. This suggests that the lowest energy barrier for diffusion requires the diffusing Li^+ to maintain a high coordination number with O^{2-} and a shorter diffusion distance, like pathway (1). This is in common with all other diffusion mechanisms (for example Li_i^+ and Li_i^0), where the knock-off mechanism involves both the

higher coordination number of Li^+ with O^{2-} and the shortest diffusion distance as compared with the direct hopping mechanism.³² Although the concentration of a neutral Li vacancy is lower than the negatively charged Li vacancy in the whole 0–4.4 V range according to Figure 2(b), we note that its diffusion follows the same path as a negatively charged Li vacancy, as shown by Chen et al.⁴⁰

C. Li Atom Interstitials. Below 0.28 V, the concentration of neutrally charged Li interstitials, Li_i^0 , becomes the second highest. Therefore, it is important to understand Li_i^0 formation and diffusion pathways. The energetically most favorable site for Li_i^0 in the Li_2CO_3 lattice is the same as that for interstitial Li_i^+ in Conf. 1 of Table 2. The distorted Li_2CO_3 lattice that results from the incorporation of the two excess interstitials (Li_i^0 or Li_i^+) into a Li_2CO_3 $2 \times 2 \times 2$ supercell is almost the same. If we overlap the atomic core positions from the two structures, all of the relative atomic core position differences are less than 0.013 Å. However, the charge distribution is different since there is one more electron in the Li_i^0 interstitial structure. By subtracting the charge density of the supercell containing one Li_i^+ interstitial from the supercell with one Li_i^0 interstitial, we obtain the charge distribution of the one electron associated with Li_i^0 . This charge density difference leads to the excess electron distribution shown in Figure 4. The purple spheres are Li ions on interstitial sites and

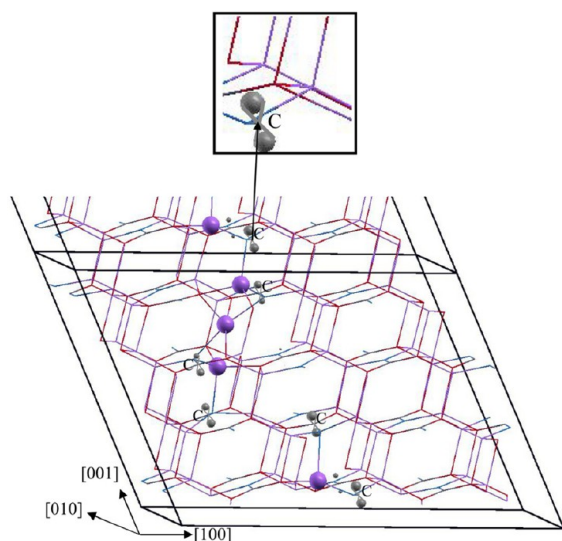
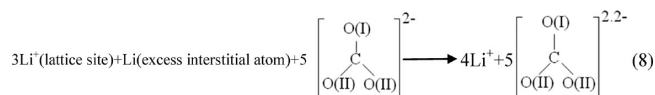


Figure 4. Isosurfaces (gray) of the differential charge density between the $2 \times 2 \times 2$ supercell with an excess interstitial Li atom and the corresponding one with an excess interstitial Li^+ . Li, C, O(I), and O(II) atoms are represented by purple, gray, blue, and red lines (spheres), respectively. The excess interstitial Li^+ and three perturbed lattice Li^+ ions are represented by four purple spheres. Values of isosurfaces are $0.028 \text{ e}/\text{\AA}^3$. Inset is the magnified drawing of the dumbbell shape.

distorted lattice sites, and they are all ionized and have $\sim +1$ net charge. This means when one Li_i^0 interstitial is introduced into Li_2CO_3 it becomes a Li ion, and one excess electron will be donated to the Li_2CO_3 lattice. The gray regions are the isosurfaces of the excess electron density of $0.028 \text{ e}/\text{\AA}^3$ shown as a dumbbell shape (or two spheres above and below the C core). The charges are mainly localized at five C atoms, with “C” labeled near the core position. These five C atoms all share O(I) with the purple Li ions (interstitial or three perturbed lattice Li^+). Thus, each of the five CO_3 groups obtains $1/5$ of extra charge, becoming $[\text{CO}_3]^{2.2-}$. The dumbbell shape of the electron

isosurface indicates that the excess electron associated with Li_i^0 starts to occupy the anti- σ orbital in the $[\text{CO}_3]^{2.2-}$ group. Consequently, the corresponding five C–O(I) bond lengths are stretched by $\sim 0.02 \text{ \AA}$. We can express this process of charge transfer and stretching of five C–O(I) bonds as the following



The diffusion process of a Li_i^0 in Li_2CO_3 is the same as the knock-off mechanism for interstitial Li_i^+ . Figure 5(a) shows a $2 \times$

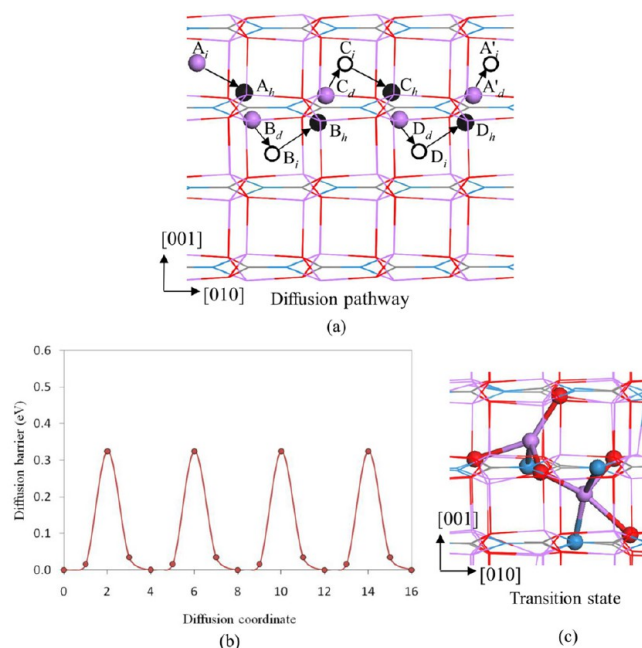


Figure 5. (a) Schematic diagram of diffusion pathway, (b) energy profile, and (c) transition state structure of the Li_i diffusion from site A_i along the $[010]$ direction following the knock-off diffusion mechanism. In all the atomic structures, the lines sketch the perfect Li_2CO_3 crystalline structure projected along the $[100]$ direction or a direct view of the dotted (100) plane in Figure 1. A_i is the initial location of the diffusing Li_i . A'_i is the periodic image of A_i . Black and hollow spheres mark sites through which Li_i diffuses. Subscripts i , d , and h refer to interstitial, distorted lattice, and nondistorted lattice sites, respectively. The initial positions of A, B, C, D, and A' (periodic image of A) are highlighted in purple spheres. These atoms take turns to be the diffusing interstitials and move in four knock-off steps: (1) $A_i \rightarrow A_h$, $B_d \rightarrow B_i$; (2) $B_i \rightarrow B_h$, $C_d \rightarrow C_i$; (3) $C_i \rightarrow C_h$, $D_d \rightarrow D_i$; (4) $D_i \rightarrow D_h$, $A'_d \rightarrow A'_i$. The end point structures after each knock-off step correspond to diffusion coordinates of 4, 8, 12, and 16 in the computed diffusion energy profile. The transition state structure corresponds to diffusion coordinate 2 in (b). The two purple spheres in the transition state in (c) are due to the simultaneous diffusion steps of $A_i \rightarrow A_h$ and $B_d \rightarrow B_i$.

2×2 Li_2CO_3 supercell with the Li_i^0 diffusion pathway, which looks very similar to Figure 3(a) in ref 32 for diffusion of Li_i^+ . The diffusion starts with an excess interstitial Li atom (actually Li^+ plus one electron distributed among five C atoms) initially located at the site A_i . Several other crystallographically equivalent interstitial sites B_i , C_i , and D_i are also labeled in Figure 5(a), and A'_i is the periodic image of the Li_i^0 at (the initial) site A_i . Subscripts i , d , and h refer to interstitial, distorted lattice, and nondistorted lattice sites, respectively. Their relationship can be understood as follows. The occurrence of an excess interstitial Li atom at site A_i (B_i , C_i , D_i are equivalent sites) causes Li^+ at a

nondistorted lattice site A_h (B_h , C_h , D_h) to relax to the distorted lattice site B_d (C_d , D_d , A'_d).

As the first step, we consider two possibilities for Li_i^0 at the interstitial site A_i to diffuse to the site B_i along $[01\bar{1}]$. The first possibility is the direct hopping of the excess Li_i^0 from site A_i to B_i along $[01\bar{1}]$. The barrier computed from CI-NEB for this process is as high as ~ 10 eV since the Li_i^0 must approach within 0.862 Å of an O^{2-} ion. Alternatively, the Li_i^0 at A_i diffuses along $[01\bar{1}]$ to a nondistorted lattice site A_h and simultaneously knocks-off an existing Li^+ at the distorted lattice site B_d to become a Li_i at the interstitial site B_i , that is, $A_i \rightarrow A_h$, $B_d \rightarrow B_i$. This knock-off process has only a net 0.32 eV energy barrier. The computed energy barrier for this concerted diffusion of Li_i^0 at A_i with lattice Li^+ at B_d from CI-NEB is substantially lower than that for direct hopping along $[01\bar{1}]$.

There are four neighboring lattice Li^+ ions within 2.417–2.647 Å of an excess interstitial Li atom in the highlighted (100) plane of Figure 1. Thus, the excess interstitial Li atom can knock-off any of the four neighboring lattice Li^+ with the same energy barriers and equivalent probabilities to effectively achieve a diffusion step along $[01\bar{1}]$, $[011]$, $[0\bar{1}1]$, or $[0\bar{1}\bar{1}]$. The net effect of the combination of these knock-off steps along four directions is macroscopic diffusion of the Li_i^0 within the (100) plane in Li_2CO_3 .

One example for such a combination is along the $[010]$ direction, as shown in Figure 5(a). A second knock-off step for continued Li_i^0 diffusion is $B_i \rightarrow B_h$, $C_d \rightarrow C_i$ in which a Li_i^0 at interstitial site B_i diffuses along $[011]$ to a nondistorted lattice site B_h and simultaneously knocks-off an existing Li^+ at the distorted lattice site C_d to become a Li_i^0 at the new interstitial site C_i . After $A_i \rightarrow A_h$, $B_d \rightarrow B_i$ and $B_i \rightarrow B_h$, $C_d \rightarrow C_i$, the Li_i^0 at site A_i has effectively diffused through a full lattice length (4.906 Å) along $[010]$ to C_i . In each step, the distances traveled by the Li ion involved in knock-off are all within 1.860–2.043 Å. The sum of these distances from the diffusing species involved in the two knock-off steps is only 4.086 Å, which is shorter than the full lattice length of 4.906 Å. Thus, the total travel distance of $A_i \rightarrow A_h$, $B_d \rightarrow B_i$ and $B_i \rightarrow B_h$, $C_d \rightarrow C_i$ is shorter than that of a straight line from A_i to C_i in Figure 5(a). After another two similar knock-off steps, $C_i \rightarrow C_h$, $D_d \rightarrow D_i$ then $D_i \rightarrow D_h$, $A'_d \rightarrow A'_i$, and the Li^+ ion at the distorted lattice site A'_d is knocked-off by Li_i at site D_i which becomes the periodic image of Li_i^0 at (the initial) site A_i in the original structure. As shown in the computed diffusion barrier profile in Figure 5(b), wherein A_i corresponds to diffusion coordinate 0, the barrier height for each knock-off step is 0.32 eV. Therefore, Li_i diffuses within the (100) plane in Li_2CO_3 with a diffusion energy barrier of 0.32 eV. Interestingly, the energy barrier for Li_i diffusion is nearly the same as that (0.31 eV) for Li_i^+ diffusion.³²

A Li_i^0 interstitial can also diffuse along the $[010]$ direction via a direct-hopping mechanism. We conducted CI-NEB calculations for direct-hopping diffusion of Li_i^0 . Results indicate that the diffusion barrier of 0.54 eV is the same as that for Li_i^+ with the direct-hopping mechanism, and it is nearly twice the 0.32 eV barrier computed for the knock-off mechanism in Figure 5. In the direct-hopping mechanism, diffusion of a full lattice length ($A_i \rightarrow C_i$, 4.906 Å) along $[010]$ requires that Li_i^+ or Li_i^0 must move 7.496 Å, which is nearly twice that required by the knock-off mechanism (4.086 Å).

The Li_i^0 in Li_2CO_3 prefers to maintain the 5-fold coordination with O not only in the equilibrium state but also during the diffusion process. In the transition state for the knock-off mechanism in Figure 5(c) (corresponding to coordination

number 2 in Figure 5(a)), the diffusing Li_i^0 (e.g., coming from site A_i) keeps 4-fold Li–O coordination (Li–O(I): 1.844 Å; Li–O(II): 1.874, 1.888, and 2.129 Å). However, the Li^+ being knocked-off (e.g., coming from site B_d) has 5-fold Li–O coordination (Li–O(I): 1.975 and 2.135 Å; Li–O(II): 1.903, 1.923, and 2.102 Å). The average Li–O bond lengths for the two moving Li in the transition state are slightly longer than the average Li–O bond lengths in the end point structures by 0.026 and 0.032 Å. In comparison, the transition state computed for the direct-hopping mechanism (not shown) has a 3-fold Li–O coordination for the diffusing Li_i^+ (Li–O(II): 1.765, 1.767, and 1.895 Å), which corresponds to the net 0.54 eV diffusion energy barrier. Note that a phonon calculation on the transition state structure yielded a single imaginary frequency, as expected.

Intuition would suggest that the diffusion barrier should be higher for the Li_i^0 than for the Li_i^+ . However, our CI-NEB calculations show that the diffusion barriers are almost the same for Li_i^0 and Li_i^+ in both the knock-off and direct-hopping diffusion mechanisms. This is likely due to the fact that Li_i^0 has fully ionized. However, a natural question is how the 2s electron from the Li_i^0 diffuses simultaneously with the ionized Li interstitial to achieve the diffusion of a neutral Li_i^+ . We tracked the location of the excess electron on the Li_2CO_3 lattice by the gray dumbbell-shaped isosurfaces in Figures 6(a)–(c). Figure

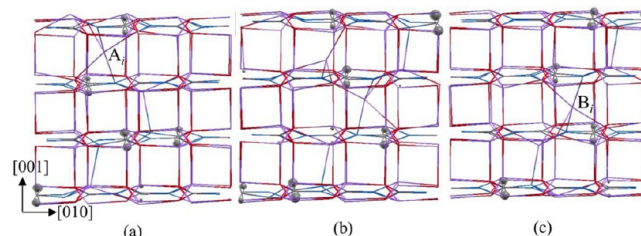


Figure 6. Isosurfaces (gray) of the differential charge density between the $2 \times 2 \times 2$ supercell with an excess Li atom and the corresponding one with an excess Li ion: (a) configuration corresponding to the site A_i in Figure 5(a) or diffusion coordinate 0 in Figure 5(b), (b) transition state configuration corresponding to diffusion coordinate 2 in Figure 5(b), and (c) configuration corresponding to the site B_i in Figure 5(a) or diffusion coordinate 4 in Figure 5(b). Li, C, O(I), and O(II) atoms are represented by purple, gray, blue, and red lines, respectively. Values of isosurfaces are 0.028 $\text{e}/\text{\AA}^3$.

6(a) shows the same configuration as Figure 4 without highlighting the Li ions. The interstitial ion, which is at the left upper corner in Figure 6(a), is coordinated with five O bonds; this is the initial configuration of A_i in Figure 5(a). Figure 6(b) is the transition state configuration, and Figure 6(c) is the ending configuration for the knock-off process of $A_i \rightarrow A_h$, $B_d \rightarrow B_i$ in Figure 5(a). For the initial and final configurations in Figures 6(a) and 6(c), the excess charge is mainly localized at the five C atoms, as discussed in Figure 4. For the transition state configuration in Figure 6(b), significant perturbation of four lattice Li^+ ions from their equilibrium lattice sites and the incorporation of an excess Li atom cause six C–O(I) bonds to be elongated by ~ 0.02 Å. Consequently, the transferred charge is mainly localized at these six C atoms. The charge transfer along with the atomic distortion is likely to be the case since it is unlikely for the polaron (ex: the excess electron on the C atoms) and the Li ion to diffuse independently in battery materials.^{64–67} However, current DFT calculations may underestimate the diffusion barrier of Li_i^0 due to the fact that LDA tends to delocalize the excess charge. Although it is unlikely to localize

one excess electron to one C atom, the charge can be shared by less (than five) C atoms with the hybrid functional. Then, stronger binding between the Li ion and the excess electrons can slow down Li_i^0 diffusion.

Although it accompanies the formation and diffusion of the excess interstitial Li atom in Li_2CO_3 , the Li_i^0 still exists as a Li_i^+ ion, but one excess electron is redistributed over C atoms which are bonded to O(I) ions coordinating with the excess interstitial Li ion and the consequently perturbed lattice Li ions. The small amount of distributed charge becomes easier to transfer between atoms with the help of C–O(I) bonds that are stretched due to the incorporation of excess interstitial Li_i^0 and its distortion of the lattice Li^+ -ion positions. Therefore, one electron diffuses along with the Li^+ interstitial as a neutral Li atom interstitial with an energy barrier as low as 0.3 eV. In other words, a diffusing Li_i^0 interstitial carries a charge with it.

D. Li Frenkel Pairs. Li Frenkel pairs are the third most important diffusion carriers (after Li_i^+ and V_{Li}^-) above 0.38 V, so we expect Frenkel pairs to diffuse in the Li_2CO_3 coated on both cathode and anode materials. A Frenkel pair is formed when Li^+ is displaced from its lattice position to a nearby interstitial site (Conf. 1 in Table 2) and creates a vacancy at its original site. Therefore, a Frenkel pair contains a Li_i^+ and a nearby V_{Li}^- . It is necessary to first locate the energetically favorable relative position of this paired defect by searching for all such pairs and then subsequently computing the energy of each. In Figure 7, the

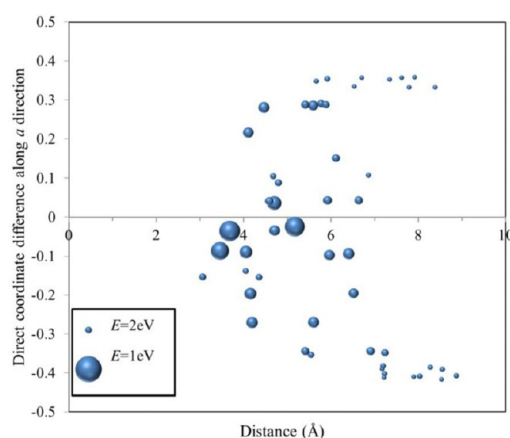


Figure 7. Dependence of Frenkel pair formation energy on the relative position between Li_i^+ and V_{Li}^- , while their absolute separation distance and the projected separation distance along the [100] direction are represented by x and y axes, respectively. The size of the spherical label is inversely proportional to the formation energy, so large spheres correspond to the lower formation energy. The lowest formation energy is for the two pairs on the same (100) plane (indicated by the near zero y values).

formation energy is inversely scaled with the spherical label size (a larger sphere size means lower formation energy), and the location of the sphere reveals the relative position of Li_i^+ and V_{Li}^- in a Frenkel pair. We show their separation distance and the separation projected along the [100] direction (zero means both are on the same (100) plane) as the two axes in Figure 7. The two energetically most favorable Frenkel pairs are formed when the Li_i^+ is either 3.681 or 5.166 Å from V_{Li}^- in the same (100) layer (see the two largest spheres adjacent to the horizontal axis in Figure 7). Furthermore, after atomic relaxation this Li_i^+ ion in the Frenkel pair also has a five-coordinated O environment with two Li–O(I) and three Li–O(II) bonds. This is very similar to the

case of an excess interstitial Li^+ ion, which becomes 5-fold coordinated interstitial Li–O in Conf. 1 of Table 2. For example, V_{Li}^- in the $2 \times 2 \times 2$ perfect Li_2CO_3 supercell in Figure 1 has a fractional coordinate of (0.4028, 0.2221, 0.3340), and the Li_i^+ in the most energetically stable Frenkel pair is located at (0.3674, 0.1388, 0.0097) or (0.3788, 0.3738, 0.7419), which is 3.681 or 5.166 Å away from the V_{Li}^- .

Our investigation of the concerted diffusion of Frenkel pairs was motivated by the diffusion of the excess interstitial Li^+ via knock-off of Li^+ at neighboring lattice sites since the interstitial Li^+ ion from a Frenkel pair and excess interstitial Li^+ ion occupy identical sites. Figure 8(a) shows a $2 \times 2 \times 2$ Li_2CO_3 supercell with the Li Frenkel pair diffusion pathway. Black and hollow spheres mark sites through which the interstitial Li^+ ion and negatively charged Li vacancy pass during diffusion. The interstitial Li^+ and the negatively charged Li vacancy are located

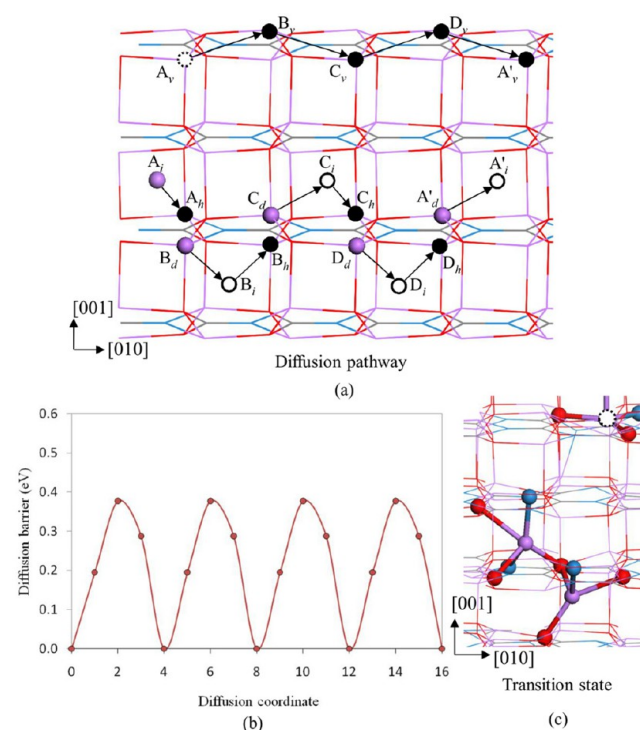


Figure 8. (a) Schematic diagram of the Li Frenkel pair diffusion pathway. (b) Diffusion barrier profile. (c) Transition state structure during Li Frenkel pair diffusion. In all the atomic structures, the lines sketch the perfect Li_2CO_3 crystalline structure projected along the [100] direction or a direct view of the dotted (100) plane in Figure 1. (A_i, A_v) is the initial location of the diffusing Li Frenkel pair. (A'_i, A'_v) is the periodic image of (A_i, A_v). Black and solid line-edged hollow spheres mark sites through which the Li Frenkel pair diffuses. Subscripts i, d, h , and v refer to interstitial, distorted lattice, nondistorted lattice, and Li vacancy sites, respectively. The initial positions of the Li vacancy and A, B, C, D , and A' (periodic image of A) are highlighted in dotline-edged hollow and purple spheres, respectively. These atoms take turns to be the diffusing interstitials and move in four knock-off steps in (a): (1) $A_v \rightarrow B_v, A_i \rightarrow A_{ih}, B_d \rightarrow B_{ij}$; (2) $B_v \rightarrow C_v, B_i \rightarrow B_{ih}, C_d \rightarrow C_{ij}$; (3) $C_v \rightarrow D_v, C_i \rightarrow C_{ih}, D_d \rightarrow D_{ij}$; (4) $D_v \rightarrow A'_v, D_i \rightarrow D_{ih}, A'_d \rightarrow A'_i$. The end point structures after each diffusion step correspond to diffusion coordinates of 4, 8, 12, and 16 (in (b)) in the computed diffusion energy profile. The transition state structure in (c) corresponds to diffusion coordinate 2 in (b). In (c), one dotline-edged hollow sphere (one oxygen coordinated with it is not shown) and two purple spheres are due to the simultaneous diffusion steps of $A_v \rightarrow B_v, A_i \rightarrow A_{ih}$ and $B_d \rightarrow B_{ij}$.

Table 4. Diffusion Energy Barrier (E_m), Formation Energy (E_f), Activation Energy Barrier for Ionic Conductivity (E_{act}), Concentration (S), Self-Diffusion Coefficient (D), and Ionic Conductivity (σ) of Li_i^+ and V_{Li}^- in Li_2CO_3 at 0.23, 0.98–3.98, and 4.28 V ($T = 300$ K), Respectively^a

voltage (V)	for each diffusion carrier							
	diffusion carrier	E_m (eV)	E_f (eV)	E_{act} (eV)	S (cm ⁻³)	D (cm ² /s)	σ (S/cm)	σ (S/cm) in Li_2CO_3
0.23	Li_i^+	0.31	0.47	0.78	5.24×10^{14}	1.10×10^{-7}	3.57×10^{-10}	3.58×10^{-10}
	V_{Li}^-	0.24	1.16	1.39	1.42×10^3	4.98×10^{-7}	4.37×10^{-21}	
0.98–3.98	Li_i^+	0.31	0.81	1.12	8.61×10^8	1.10×10^{-7}	5.87×10^{-16}	3.25×10^{-15}
	V_{Li}^-	0.24	0.81	1.05	8.61×10^8	4.98×10^{-7}	2.66×10^{-15}	
4.28	Li_i^+	0.31	0.92	1.23	1.21×10^7	1.10×10^{-7}	8.22×10^{-18}	1.90×10^{-13}
	V_{Li}^-	0.25	0.70	0.95	6.16×10^{10}	4.99×10^{-7}	1.90×10^{-13}	
bulk Li_2CO_3 ^b				1.06 (473 K < T < 773 K)				$\sim 10^{-10}$ ($T = 298$ K)
bulk Li_2CO_3 ^c				0.77 (348 K < T < 553 K)				$\sim 2 \times 10^{-7}$ ($T = 473$ K)

^aAvailable experimental values of D and σ are also listed. ^bRef 70. ^cRef 71.

at sites A_i and A_v (denoted as the coordinate (A_i, A_v)), respectively, and they are separated from each other by 3.681 Å. Along the diffusion pathway, we show four more equivalent Frenkel pair locations, (B_i, B_v), (C_i, C_v), (D_i, D_v), (A'_i, A'_v), corresponding to the energy valleys at diffusion coordinates 4, 8, 12, and 16 in Figure 8(b). Note that in the coordinates (B_i, B_v) and (D_i, D_v) the distance between the Li_i^+ and V_{Li}^- is 3.681 Å due to the periodicity of the supercell along the [001] direction.

To further show the diffusion details, we mark subscripts i, d, h , and v in Figure 8(a) to refer to interstitial, distorted lattice, nondistorted lattice, and vacant lattice sites, respectively. Their relationship can be understood as follows. The removal of a Li^+ at the lattice site A_v , and thus its occurrence at an interstitial site A_i , causes Li^+ at the nondistorted lattice site A_h to relax to the distorted lattice site B_d by shifting 1.121 Å. The Li^+ at interstitial site A_i diffuses along [011] to a nondistorted lattice site A_h and simultaneously knocks-off an existing Li^+ at the distorted lattice site B_d to the new interstitial site B_i . At the same time, the vacancy moves along the [010] direction (similar to pathway (2) in Figure 3), that is, $A_v \rightarrow B_v, A_i \rightarrow A_h, B_d \rightarrow B_i$. As shown in Figure 8(b), this diffusion process has a net 0.377 eV energy barrier. The diffusion of a Frenkel pair includes correlated motions of a V_{Li}^- along [010] and a Li_i^+ knocking-off Li^+ at lattice sites. However, the diffusion barrier for a Li Frenkel pair is much less than the sum of the diffusion barriers of the individual carriers (e.g., 0.394 eV for a vacancy along pathway (2) in Figure 3 and 0.31 eV for excess Li^+ interstitial knock-off diffusion). Although the diffusion process of a Li Frenkel pair involves the simultaneous diffusion of a Li_i^+ and a V_{Li}^- , it requires not much more energy than a Li_i^+ diffusion and even less energy than diffusing V_{Li}^- . When Li interstitials and vacancies are far apart (in a dilute concentration, for example), they diffuse separately; however, once a Li Frenkel pair is formed (when Li_i^+ and V_{Li}^- are either 3.681 or 5.166 Å apart), their energetics are such that they diffuse together.

Due to this correlated motion, the diffusion direction for a Li Frenkel pair is limited. In Figure 8(a), the Frenkel pair will continue to diffuse along the [010] direction after the first step, i.e., $B_v \rightarrow C_v, B_i \rightarrow B_h, C_d \rightarrow C_i$. The diffusion barrier is still 0.377 eV for this step. After these two steps, the Li Frenkel pair with the coordinate (A_i, A_v) has effectively diffused through a full length (4.906 Å) along [010] to (C_i, C_v). In each step, the distances traveled by the Li vacancy, interstitial Li^+ ion, and lattice Li^+ are 2.764, 1.915, and 1.781 Å, respectively. After another two similar steps, $C_v \rightarrow D_v, C_i \rightarrow C_h, D_d \rightarrow D_i$ then $D_v \rightarrow A'_v, D_i \rightarrow D_h, A'_d \rightarrow A'_i$, the Li^+ at the distorted lattice site A'_d is knocked-off by Li^+ at site D_i and becomes the periodic image of Li^+ at (the initial) site A_i in the Li_2CO_3 lattice.

The transition state structure associated with diffusion of a Li Frenkel pair is plotted in Figure 8(c). The configurations of the two Li^+ involved in the knock-off mechanism of the Li interstitials are very similar to that of the excess Li interstitial. It is characterized by the feature that the coordination numbers of the two moving Li^+ species with O ions are either 5 or 4. The Li–O bond lengths are 1.950 and 2.329 Å (Li–O(I)), 1.898, 1.931, and 2.228 Å (Li–O(II)) for the interstitial Li^+ ion, and 1.881 (Li–O(I)), 1.892, 1.901, and 2.061 Å (Li–O(II)) for the lattice Li^+ ion. However, the location of the diffusing Li, when it switches positions with the vacancy, is different than that for a vacancy in pathway (2) in Figure 3. At the transition state for vacancy diffusion, the diffusing Li is close to the middle point of the $A_v \rightarrow B_v$ movement. However, during its correlated motion in a Frenkel pair, the vacancy has already jumped to location of B_v at the transition state.

Diffusion of the Li Frenkel pair with the Li_i^+ and V_{Li}^- separated from each other by 5.166 Å also follows the motion of the Li vacancy between neighboring Li lattice sites along the [010] direction and the knock-off of a Li^+ at a lattice site and has a net 0.377 eV energy barrier. The motion of the interstitial and vacancy in a Frenkel pair is highly correlated. It is therefore not surprising that no other feasible diffusion pathways have been found via CI-NEB calculations. In some cases, especially when it does not diffuse along [010] in the (001) plane, a Frenkel pair can be annihilated back to part of the Li_2CO_3 lattice. In some other cases, the energy barrier is too high, so diffusion cannot occur. For example, direct hopping of an interstitial Li^+ from site A_i to B_i with the vacancy jumping from A_v to B_v requires an energy barrier of ~ 10 eV.

3.3. Discussion on the Effect of Voltage on Ionic Conduction in Li_2CO_3 . Self-diffusion coefficients for a defect i at charge state q in Li_2CO_3 can be computed via^{68,69}

$$D(i, q) = \frac{1}{2} \nu^* (\Delta x)^2 \exp^{-(E_m(i, q)/k_B T)} \quad (9)$$

where $E_m(i, q)$ is the diffusion energy barrier associated with defect i in Section 3.2; ν^* is the lattice vibrational frequency ($\sim 10^{13}$ Hz estimated from our phonon calculations); and Δx is the net distance for each diffusion step (4.906 Å for the Li_i^+ and 2.974 Å for the V_{Li}^-).

Given that the concentration of defect i in Li_2CO_3 is dilute, the defect can move through diffusion (driven by a concentration gradient) and migration (driven by an electric potential gradient). We computed both $D(i, q)$ (see eq 9) and $S(i, q)$ (Figure 3(b)) with DFT. The ionic conductivity, $\sigma(i, q)$, is calculated from the Nernst–Einstein equation

$$\sigma(i, q) = \frac{F^2 q^2 D(i, q) S(i, q)}{RT} \quad (10)$$

Thus, the activation energy for the ionic conductivity, $E_{\text{act}}(i, q)$, of the defect i , includes both its formation energy and its diffusion barrier, i.e.

$$E_{\text{act}}(i, q) = E_{\text{m}}(i, q) + E_{\text{f}}(i, q) \quad (11)$$

From eqs 9–11, we can compute E_{m} , E_{f} , E_{act} , S , D , and σ of Li_i^+ and V_{Li}^- in Li_2CO_3 at different voltage values at room temperature ($T = 300$ K). As discussed in Section 3.2, voltage refers to the open circuit voltage value of the negative (or positive) electrode relative to Li metal (Li^+/Li). These parameters are listed in Table 4 at selected voltages.

At low voltages (0–0.98 V), Li_i^+ dominates ionic conduction in Li_2CO_3 . For example, at 0.23 V the activation energy is 0.78 V for Li_i^+ which is nearly one-half of that for V_{Li}^- (1.41 eV), although their diffusion energy barriers and self-diffusion coefficients are comparable. Consequently, the contribution of V_{Li}^- (4.374×10^{-21} S/cm) to the ionic conduction in Li_2CO_3 is negligible relative to that of the Li_i^+ (3.574×10^{-10} S/cm). The formation of Li_i^+ is energetically more favorable at low voltages as shown in Figure 2. However, at voltages ranging from 0.98 to 3.98 V, the Li_i^+ and V_{Li}^- contributions to ionic conduction in Li_2CO_3 are comparable (since the formation energies for the Li_i^+ and V_{Li}^- are the same) and thus both are dominant diffusion carriers in Li_2CO_3 . Alternatively, the data in Table 4 suggest that the voltage can affect not only the type of dominant diffusion carrier in Li_2CO_3 but also the ionic conductivity. The ionic conductivity σ at 0.23 V is five orders of magnitude higher than for voltages ranging from 0.98 to 3.98 V. At 4.28 V, the contribution of V_{Li}^- to the ionic conductivity is 10^5 times higher than that from Li_i^+ .

Regarding experimental studies, the ionic conductivities of Li_2CO_3 at temperatures ranging from 473 to 773 K and from 348 to 553 K were determined from impedance measurements in refs 70 and 71. In these experiments, a linear fit of the experimental points to an Arrhenius equation gave average activation energies of 1.06 and 0.77 eV, respectively. Note that the experimental value of 10^{-10} S/cm at $T = 298$ K in Table 4 was obtained by extrapolating the $\ln(\sigma T)$ versus $1/T$ plot in ref 70. Although refs 70 and 71 did not specify a dominant diffusion carrier, the given E_{act} and σ can be compared with our calculated values.

The changes of diffusion carriers and ionic conductivity as a function of voltage are mapped in Figure 9 for the overall battery range from 0 to 4.4 V. Although Li_2CO_3 can exist as part of an SEI film on anode and cathode surfaces simultaneously, the

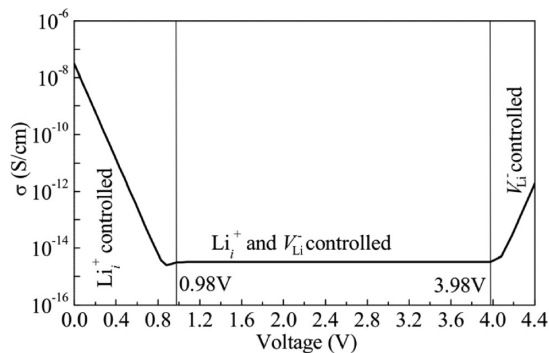


Figure 9. Li^+ transport map in Li_2CO_3 as a function of the voltage of nearby electrode materials referenced to Li metal (zero voltage).

dominant diffusion carriers and ionic conductivities at both locations are quite different from one another. For Li_2CO_3 on an anode, one can take the data below 0.4 V and find that excess Li^+ interstitial is the dominant diffusion carrier. For Li_2CO_3 on typical cathode materials, the voltage changes from ~ 3 to 4.2 V (e.g., spinel LiMn_2O_4 , layered LiNiO_2 , LiCoO_2 , or $\text{LiNi}_{1-x}\text{Co}_x\text{Al}_y\text{O}_2$); Li^+ transport is controlled by either vacancy diffusion alone or the diffusion of both vacancy and interstitial Li (moving independently). As a result, the Li^+ conductivity is above 10^{-11} (up to 10^{-8}) S/cm in Li_2CO_3 on graphite but below 10^{-13} (down to 10^{-15}) S/cm for Li_2CO_3 on typical cathode surfaces. This order of magnitude difference in Li^+ conductivity may explain why there has been some disagreement as to whether or not Li_2CO_3 is a good Li conductor for Li-ion batteries.^{14,17,32,42,43,45}

Another insight we gained from our calculations is that diffusion of a Li_i^0 interstitial carries a charge with it. This process has complicated implications for degradation in Li-ion batteries. If a Li_i^0 exists in Li_2CO_3 and is able to diffuse easily, as we predicted in Section 3.2.2.C, it will carry an electron from the graphite phase through the Li_2CO_3 and SEI, and hence Li_i^0 will get into the electrolyte phase. If Li^+ ions and electrons recombine to make Li^0 at the top surface of the SEI, i.e., adjacent to the electrolyte, those Li atoms would react with ethylene carbonate (a common Li-ion battery electrolyte) within picoseconds to form additional SEI according to Leung's calculations.²⁴ Thus, we expect that Li_i^0 transport will lead to self-discharge and irreversible capacity loss. In fact, Yazami and Reynier⁷² developed a model involving the formation of an adsorbed electron-ion–solvent complex on a graphite surface as the mechanism of self-discharge. However, no mechanism of Li^+ –electron diffusion was ever proposed. We believe that our calculations demonstrate a feasible mechanism for the formation and diffusion of Li_i^0 in an SEI film. According to Figure 2, the concentration of Li_i^0 increases with decreasing voltage; therefore, the self-discharging process will be intensified at lower voltages, which is in agreement with experiments.⁷²

4. CONCLUSIONS

Li^+ -associated defect thermodynamics have been computed with DFT, CI-NEB, and the supercell method to lattice dynamics, over a 0–4.4 V range. Defect diffusion mechanisms in Li_2CO_3 were identified along with the dominant diffusion carriers. We quantified the dependence of the defect formation energy and concentration on the voltage relative to Li metal (0 V). We predicted that the dominant diffusion carrier in Li_2CO_3 below the voltage range of SEI film formation on an anode surface is excess interstitial Li^+ . However, in the Li_2CO_3 formed on a cathode surface, the Li^+ vacancies become equally important as interstitial Li^+ by having the same concentrations, but the Li^+ vacancies eventually become the dominant diffusion carrier above ~ 4 V. The diffusion pathways and barriers for the dominant diffusion carriers were computed, from which some important conclusions about the effect of voltage on the lithium ionic conductivity in Li_2CO_3 could be drawn. The Li^+ conductivity in Li_2CO_3 first drops from 10^{-8} to $\sim 10^{-15}$ S/cm when the voltage of the material coated by Li_2CO_3 changes from 0 to 0.98 V; the conductivity remains a constant until 3.98 V at which point it rises up to $\sim 10^{-12}$ S/cm until it will be decomposed (into Li_2O and CO_2) under higher voltage. While most Li_i^+ and V_{Li}^- diffuse independently, they can form a Li Frenkel pair when their distance is close to about 3–5 Å on the same (100) plane. The motion of the interstitial and vacancy in a Frenkel pair is highly

correlated along [010] in the (001) plane. A possible mechanism is also proposed to explain electron leakage through an SEI film into the electrolyte by the diffusion of Li_i^0 interstitials. Li_i^0 interstitials diffuse via a knock-off mechanism, which is that same as that for Li_i^+ , but when Li_i^0 diffuses, the dissociated electron is distributed on the nearby carbon atoms and diffuses along with the diffusing Li_i^+ . Increasing the diffusion carriers' concentrations will efficiently increase Li^+ transport through crystalline Li_2CO_3 and improve battery rate performance. Since our calculations demonstrate that the diffusion carriers' concentration is strongly voltage-dependent, we suggest different dopants for anode and cathode materials that may increase Li conductivity through Li_2CO_3 . For example, doping Li_2CO_3 with BO_3^{3-} replacing CO_3^{2-} will increase Li-ion interstitial concentration and thus improve the ionic conductivity in the Li_2CO_3 on an anode surface. Doping Ca^{2+} , Mg^{2+} , Al^{3+} or La^{3+} will increase Li-ion vacancies, thereby enhancing Li conductivity in the Li_2CO_3 on the cathode surface.

AUTHOR INFORMATION

Corresponding Author

*E-mail: yue.qi@gm.com.

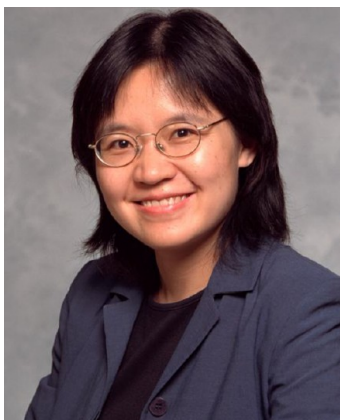
Notes

The authors declare no competing financial interest.

Biographies



Dr. Siqi Shi obtained his B.S. from Jiangxi Normal University in 1998. He finished his Ph.D. from Institute of Physics, Chinese Academy of Sciences, in 2004. After that, he had worked at the National Institute of Advanced Industrial Science and Technology of Japan and Brown University of USA as a senior research associate until joining Shanghai University as a professor in 2013. Shi's research interests focus on the first-principles calculations of energy storage and conversion materials related to lithium-ion battery and CeO_2 -based solid-state oxide fuel cell.



Dr. Yue Qi is a Staff Research Scientist working on computational materials sciences at the Chemical and Materials Systems Lab, General Motors R&D Center, Warren, MI. She joined GM right after she obtained her Ph.D. in Materials Science with a minor in Computer Science from Caltech in 2001. She uses a multiscale modeling approach to solve chemical–mechanical coupling in materials related to batteries, fuel cells, and vehicle light-weighting. She has received three GM Campbell Research Awards on “fundamentals of tribology”, “high temperature forming of Aluminum”, and “nano-scale plasticity”. Her most recent research topic is on the integration of material properties into Li-ion battery failure modeling.



Dr. Hong Li is a staff scientist in Institute of Physics, Chinese Academy of Sciences since 1999. His research interests include materials for high energy density lithium batteries and fundamental understanding on transport, storage, and reaction of ions in solids.



Dr. Louis G. Hector, Jr. is a Technical Fellow working on both computational and experimental materials science in the Chemical and Materials Systems Lab, General Motors R&D Center. He joined GM in early 2001 after nearly 14 years at Alcoa Technical Center. In addition to his interests in applying first-principles techniques to compute a wide array of energy material properties and behavior, he also uses stereo digital image correlation to measure deformation of materials from quasi-static to low dynamic strain rates. He is a PI on a recent DOE award for Integrated Computational Materials Engineering (ICME) of third generation advanced high strength steels.

ACKNOWLEDGMENTS

The authors wish to express their gratitude to Drs. Chen Li, Steve Harris, Bob Powell, and Mark Verbrugge for their careful review of the manuscript and insightful suggestions. The staff of the High Performance Computing Center at General Motors is acknowledged for computer hardware resources. Additional

computational resources, networking, and support were provided by GM Information Systems and Services.

REFERENCES

- (1) Tarascon, J. M.; Armand, M. Issues and Challenges Facing Rechargeable Lithium Batteries. *Nature* **2001**, *414*, 359–367.
- (2) Whittingham, M. S. Lithium Batteries and Cathode Materials. *Chem. Rev.* **2004**, *104*, 4271–4301.
- (3) Armand, M.; Tarascon, J. M. Building Better Batteries. *Nature* **2008**, *451*, 652–657.
- (4) Ellis, B. L.; Lee, K. T.; Nazar, L. F. Positive Electrode Materials for Li-Ion and Li-Batteries. *Chem. Mater.* **2010**, *22*, 691–714.
- (5) Zu, C. X.; Li, H. Thermodynamic Analysis on Energy Densities of Batteries. *Energy Environ. Sci.* **2011**, *4*, 2614–2624.
- (6) Manthiram, A. Materials Challenges and Opportunities of Lithium Ion Batteries. *J. Phys. Chem. Lett.* **2012**, *2*, 176–184.
- (7) Goodenough, J. B.; Kim, Y. Challenges for Rechargeable Li Batteries. *Chem. Mater.* **2010**, *22*, 587–603.
- (8) Aurbach, D.; Ein-Eli, U.; Chusid, O.; Carmeli, Y.; Babai, M.; Yamin, H. The Correlation between the Surface-Chemistry and the Performance of Li-Carbon Interaction Anodes for Rechargeable Rocking-Chair Type Batteries. *J. Electrochem. Soc.* **1994**, *141*, 603–611.
- (9) Aurbach, D.; Markovsky, B.; Shechter, A.; Ein-Eli, Y.; Cohen, H. A Comparative Study of Synthetic Graphite and Li Electrodes in Electrolyte Solutions Based on Ethylene Carbonate Dimethyl Carbonate Mixtures. *J. Electrochem. Soc.* **1996**, *143*, 3809–3820.
- (10) Arora, P.; White, R. E.; Doyle, M. Capacity Fade Mechanisms and Side Reactions in Lithium-Ion Batteries. *J. Electrochem. Soc.* **1998**, *145*, 3647–3667.
- (11) *Advances in Lithium-Ion Batteries*; van Schalkwijk, W. A., Scrosati, B., Ed.; Kluwer: New York, 2002.
- (12) *Lithium-Ion Batteries: Solid-Electrolyte Interphase*; Wang, Y., Balbuena, P. B., Ed.; Imperial College: London, 2004.
- (13) Xu, K. Nonaqueous Liquid Electrolytes for Lithium-Based Rechargeable Batteries. *Chem. Rev.* **2004**, *104*, 4303–4417.
- (14) Zhuang, G. V.; Chen, G.; Shim, J.; Song, X.; Ross, P. N.; Richardson, T. J. Li_2CO_3 in $\text{LiNi}_{0.8}\text{Co}_{0.15}\text{Al}_{0.05}\text{O}_2$ Cathodes and Its Effects on Capacity and Power. *J. Power Sources* **2004**, *134*, 293–297.
- (15) Liu, N.; Li, H.; Wang, Z. X.; Huang, X. J.; Chen, L. Q. Origin of Solid Electrolyte Interphase on Nanosized LiCoO_2 . *Electrochem. Solid-State Lett.* **2006**, *9*, A328–A331.
- (16) Aurbach, D.; Markovsky, B.; Salitra, G.; Markevich, E.; Talyossef, Y.; Koltypin, M.; Nazar, L.; Ellis, B.; Kovacheva, D. Review on Electrode-Electrolyte Solution Interactions, Related to Cathode Materials for Li-Ion Batteries. *J. Power Sources* **2007**, *165*, 491–499.
- (17) Winter, M. The Solid Electrolyte Interphase-The Most Important and the Least Understood Solid Electrolyte in Rechargeable Li Batteries. *Z. Phys. Chem.* **2009**, *223*, 1395–1406.
- (18) Wang, C.; Kakwan, I.; Appleby, A. J.; Little, F. E. In Situ Investigation of Electrochemical Lithium Intercalation into Graphite Powder. *J. Electroanal. Chem.* **2000**, *489*, 55–67.
- (19) Zhang, J.; Wang, R.; Yang, X. C.; Lu, W.; Wu, X. D.; Wang, X. P.; Li, H.; Chen, L. W. Direct Observation of Inhomogeneous Solid Electrolyte Interphase on MnO Anode with Atomic Force Microscopy and Spectroscopy. *Nano Lett.* **2012**, *12*, 2153–2157.
- (20) Elam, J. W.; Dasgupta, N. P.; Prinz, F. B. ALD for Clean Energy Conversion, Utilization, and Storage. *MRS Bull.* **2011**, *36*, 899–906.
- (21) Marichy, C.; Bechelany, M.; Pinna, N. Atomic Layer Deposition of Nanostructured Materials for Energy and Environmental Applications. *Adv. Mater.* **2012**, *24*, 1017–1032.
- (22) Jung, Y. S.; Cavanagh, A. S.; Leah, R. A.; Kang, S. H.; Dillon, A. C.; Groner, M. D.; George, S. M.; Lee, Y. H. Ultrathin Direct Atomic Layer Deposition on Composite Electrodes for Highly Durable and Safe Li-Ion Batteries. *Adv. Mater.* **2010**, *22*, 2172–2176.
- (23) Xiao, X. C.; Lu, P.; Ahn, D. Ultrathin Multifunctional Oxide Coatings for Lithium Ion Batteries. *Adv. Mater.* **2011**, *23*, 3911–3915.
- (24) Leung, K.; Qi, Y.; Zavadil, K. R.; Jung, Y. S.; Dillon, A. C.; Cavanagh, A. S.; Lee, S. H.; George, S. M. Using Atomic Layer Deposition to Hinder Solvent Decomposition in Lithium Ion Batteries: First-Principles Modeling and Experimental Studies. *J. Am. Chem. Soc.* **2011**, *133*, 14741–14754.
- (25) Verma, P.; Maire, P.; Novák, P. A Review of the Features and Analyses of the Solid Electrolyte Interphase in Li-Ion Batteries. *Electrochim. Acta* **2010**, *22*, 6332–6341.
- (26) Aurbach, D. Review of Selected Electrode-Solution Interactions which Determine the Performance of Li and Li Ion Batteries. *J. Power Sources* **2000**, *89*, 206–218.
- (27) Zhang, S. S. A Review on Electrolyte Additives for Lithium-Ion Batteries. *J. Power Sources* **2006**, *162*, 1379–1394.
- (28) Xu, K. Electrolytes and Interphasial Chemistry in Li Ion Devices. *Energies* **2010**, *3*, 135–154.
- (29) Bhattacharya, S.; Riahi, A. R.; Alpas, A. T. A Transmission Electron Microscopy Study of Crack Formation and Propagation in Electrochemically Cycled Graphite Electrode in Lithium-Ion Cells. *J. Power Sources* **2011**, *196*, 8719–8727.
- (30) Dollé, M.; Grugeon, S.; Beaudoin, B.; Dupont, L.; Tarascon, J. -M. In Situ TEM Study of the Interface Carbon/Electrolyte. *J. Power Sources* **2001**, *97–98*, 104–106.
- (31) Shim, J.; Kostecki, R.; Richardson, T.; Song, X.; Striebel, K. A. Electrochemical Analysis for Cycle Performance and Capacity Fading of a Lithium-Ion Battery Cycled at Elevated Temperature. *J. Power Sources* **2002**, *112*, 222–230.
- (32) Shi, S. Q.; Lu, P.; Liu, Z. Y.; Qi, Y.; Hector, L. G., Jr.; Li, H.; Harris, S. J. Direct Calculation of Li-Ion Transport in the Solid Electrolyte Interphase. *J. Am. Chem. Soc.* **2012**, *134*, 15476–15487.
- (33) Lu, P.; Harris, S. J. Lithium Transport within the Solid Electrolyte Interphase. *Electrochem. Commun.* **2011**, *13*, 1035–1037.
- (34) Matsumoto, K.; Kuzuo, R.; Takeya, K.; Yamanaka, A. Effects of CO_2 in Air on Li Deintercalation from $\text{LiNi}_{1-x-y}\text{Co}_x\text{Al}_y\text{O}_2$. *J. Power Sources* **1999**, *81–82*, 558–561.
- (35) Fedorov, I. A.; Zhuravlev, Y. N.; Korabel'nikov, D. V. Band Structure and Chemical Bond in Alkali Metal Carbonates. *Russ. Phys. J.* **2006**, *49*, 1106–1111.
- (36) Zhuravlev, Y. N.; Fedorov, I. A. The Nature of Electronic States and Chemical Bonding in Lithium and Potassium Carbonates. *J. Struct. Chem.* **2006**, *47*, 206–210.
- (37) Bruno, M.; Prencipe, M. Ab Initio Quantum-Mechanical Modeling of the (001), (−101) and (110) Surfaces of Zabuyelite (Li_2CO_3). *Surf. Sci.* **2007**, *601*, 3012–3019.
- (38) Duan, Y.; Sorescu, D. C. Density Functional Theory Studies of the Structural, Electronic, and Phonon Properties of Li_2O and Li_2CO_3 : Application to CO_2 Capture Reaction. *Phys. Rev. B* **2009**, *79*, 014301(1)–014301(18).
- (39) Iddir, H.; Curtiss, L. A. Li Ion Diffusion Mechanisms in Bulk Monoclinic Li_2CO_3 Crystals from Density Functional Studies. *J. Phys. Chem. C* **2010**, *114*, 20903–20906.
- (40) Chen, Y. C.; Ouyang, C. Y.; Song, L. J.; Sun, Z. L. Electrical and Lithium Ion Dynamics in Three Main Components of Solid Electrolyte Interphase from Density Functional Theory Study. *J. Phys. Chem. C* **2011**, *115*, 7044–7049.
- (41) Shang, S. -L.; Hector, L. G., Jr.; Shi, S. Q.; Qi, Y.; Wang, Y.; Liu, Z. K. Lattice Dynamics, Thermodynamics and Elastic Properties of Monoclinic Li_2CO_3 from Density Functional Theory. *Acta Mater.* **2012**, *60*, S204–S216.
- (42) Mizusaki, J.; Tagawa, H.; Saito, K.; Uchida, K.; Tezuka, M. Lithium Carbonate as a Solid Electrolyte. *Solid State Ionics* **1992**, *53–56*, 791–797.
- (43) Christensen, J.; Newman, J. A Mathematical Model for the Lithium-Ion Negative Electrode Solid Electrolyte Interphase. *J. Electrochem. Soc.* **2004**, *151*, A1977–A1988.
- (44) Mosqueda, H. A.; Vazquez, C.; Bosch, P.; Pfeiffer, H. Chemical Sorption of Carbon Dioxide (CO_2) on Lithium Oxide (Li_2O). *Chem. Mater.* **2006**, *18*, 2307–2310.
- (45) Kobayashi, H.; Shikano, M.; Koike, S.; Sakaebe, H.; Tatsumi, K. Investigation of Positive Electrodes after Cycle Testing of High-Power Li-Ion Battery Cells I. An Approach to the Power Fading Mechanism Using XANES. *J. Power Sources* **2007**, *174*, 380–386.

- (46) Kresse, G.; Furthmüller, J. Efficient Iterative Schemes for Ab Initio Total-Energy Calculations Using a Plane-Wave Basis Set. *Phys. Rev. B* **1996**, *54*, 11169–11186.
- (47) Blöchl, P. E. Projector Augmented-Wave Method. *Phys. Rev. B* **1994**, *50*, 17953–17979.
- (48) Ceperley, D. M.; Alder, B. J. Ground State of the Electron Gas by a Stochastic Method. *Phys. Rev. Lett.* **1980**, *45*, 566–569.
- (49) Perdew, J. P.; Zunger, A. Self-Interaction Correction to Density-Functional Approximations for Many-Electron Systems. *Phys. Rev. B* **1981**, *23*, 5048–5079.
- (50) Idemoto, Y.; Richardson, J. W.; Koura, N.; Kohara, S.; Loong, C. K. Crystal Structure of $(\text{Li}_x\text{K}_{1-x})_2\text{CO}_3$ ($x = 0, 0.43, 0.5, 0.62, 1$) by Neutron Powder Diffraction Analysis. *J. Phys. Chem. Solids* **1998**, *59*, 363–376.
- (51) Monkhorst, H. J.; Pack, J. D. Special Points for Brillouin-Zone Integrations. *Phys. Rev. B* **1976**, *13*, 5188–5192.
- (52) Perdew, J. P.; Burke, K.; Ernzerhof, M. Generalized Gradient Approximation Made Simple. *Phys. Rev. Lett.* **1996**, *77*, 3865–3868.
- (53) Parlinski, K.; Li, Z. Q.; Kawazoe, Y. First-Principles Determination of the Soft Mode in Cubic ZrO_2 . *Phys. Rev. Lett.* **1997**, *78*, 4063–4066.
- (54) Parlinski, K. Software PHONON as Implemented in MedeA 2.8; Materials Design: Angel Fire, NM, 2008.
- (55) Hector, L. G., Jr.; Herbst, J. F.; Wolf, W.; Saxe, P.; Kresse, G. *Ab Initio* Thermodynamic and Elastic Properties of Alkaline-Earth Metals and Their Hydrides. *Phys. Rev. B* **2007**, *76*, 014121(1)–014121(18).
- (56) Leslie, M.; Gillan, M. J. The Energy and Elastic Dipole Tensor of Defects in Ionic Crystals Calculated by the Supercell Method. *J. Phys. C: Solid State Phys.* **1985**, *18*, 973–982.
- (57) Zhang, S. B.; Northrup, J. E. Chemical Potential Dependence of Defect Formation Energies in GaAs: Application to Ga Self-Diffusion. *Phys. Rev. Lett.* **1991**, *67*, 2339–2342.
- (58) Henkelman, G.; Uberuaga, B. P.; Jonsson, H. A Climbing Image Nudged Elastic Band Method for Finding Saddle Points and Minimum Energy Paths. *J. Chem. Phys.* **2000**, *113*, 9901–9904.
- (59) Pulay, P. Convergence Acceleration of Iterative Sequences. the Case of SCF Iteration. *Chem. Phys. Lett.* **1980**, *73*, 393–398.
- (60) Verbrugge, M. W.; Baker, D. R.; Koch, B. J. Mathematical Modeling of High-Power-Density Insertion Electrodes for Lithium Ion Batteries. *J. Power Sources* **2002**, *110*, 295–309.
- (61) Qi, Y.; Guo, H.; Hector, L. G., Jr.; Timmons, A. Threefold Increase in the Young's Modulus of Graphite Negative Electrode during Lithium Intercalation. *J. Electrochem. Soc.* **2010**, *157*, A558–A566.
- (62) Dahn, J. R. Phase Diagram of Li_xC_6 . *Phys. Rev. B* **1991**, *44*, 9170–9177.
- (63) Wang, R.; Yu, X. Q.; Bai, J. M.; Li, H.; Huang, X. J.; Chen, L. Q.; Yang, X. Q. Electrochemical Decomposition of Li_2CO_3 in $\text{NiO-Li}_2\text{CO}_3$ Nanocomposite Thin Film and Powder Electrodes. *J. Power Sources* **2012**, *218*, 113–118.
- (64) Maxisch, T.; Zhou, F.; Ceder, G. *Ab Initio* Study of the Migration of Small Polarons in Olivine Li_xFePO_4 and Their Association with Lithium Ions and Vacancies. *Phys. Rev. B* **2006**, *73*, 104301(1)–104301(6).
- (65) Ouyang, C. Y.; Du, Y. L.; Shi, S. Q.; Lei, M. S. Small Polaron Migration in $\text{Li}_x\text{Mn}_2\text{O}_4$: From First Principles Calculations. *Phys. Lett. A* **2009**, *373*, 2796–2799.
- (66) Ouyang, C. Y.; Shi, S. Q.; Lei, M. S. Jahn–Teller Distortion and Electronic Structure of LiMn_2O_4 . *J. Alloys Compd.* **2009**, *474*, 370–374.
- (67) Nie, Z. X.; Ouyang, C. Y.; Chen, J. Z.; Zhong, Z. Y.; Du, Y. L.; Liu, D. S.; Shi, S. Q.; Lei, M. S. First Principles Study of Jahn–Teller Effects in Li_xMnPO_4 . *Solid State Commun.* **2010**, *150*, 40–44.
- (68) Van der Ven, A.; Yu, H. –C.; Ceder, G.; Thornton, K. Vacancy Mediated Substitutional Diffusion in Binary Crystalline Solids. *Prog. Mater. Sci.* **2010**, *55*, 61–105.
- (69) Van der Ven, A.; Ceder, G.; Asta, M.; Tepesch, P. D. First-Principles Theory of Ionic Diffusion with Nondilute Carriers. *Phys. Rev. B* **2001**, *64*, 184307(1)–184307(17).
- (70) Dissanayake, M. A. K. L.; Mellander, B. –E. Phase Diagram and Electrical Conductivity of the $\text{Li}_2\text{SO}_4\text{–Li}_2\text{CO}_3$ System. *Solid State Ionics* **1986**, *21*, 279–285.
- (71) Shannon, R. D.; Taylor, B. E.; English, A. D.; Berzins, T. New Li Solid Electrolytes. *Electrochim. Acta* **1977**, *22*, 783–796.
- (72) Yazami, R.; Reynier, Y. F. Mechanism of Self-Discharge in Graphite–Lithium Anode. *Electrochim. Acta* **2002**, *47*, 1217–1223.